PARTICLE PRECIPITATION INDUCED BY SHORT-DURATION VLF WAVES IN THE MAGNETOSPHERF

U. S. Inan, T. F. Bell, and H. C. Chang

Radioscience Laboratory, Stanford University, Stanford, California 94305

Abstract. An extension of a previous test particle simulation model (Inan et al., 1978) of the gyroresonance wave-particle interaction in the magnetosphere is used to compute the detailed time variation of the precipitated energy flux induced by monochormatic short-duration VLF waves. The resulting precipitation pulse is found to have a characteristic shape dependent on the L value, cold plasma density, wave frequency, and duration, as well as the energetic particle distribution function. The role of these variables in determining the temporal variation and the magnitude of the precipitated flux is discussed for a wide range of typical magnetospheric parameters. As an example, a 400-m s wave pulse with a frequency of 6.825 kHz (equatorial half-gyrofrequency) at L = 4 and for a cold plasma density of 400 el/cc produces a 3.5-s long precipitation pulse as observed at 1000 km, with the flux reaching its peak value at approximately 3.8 s after the injection of the wave at the same point. Our findings indicate that if the predicted temporal variations can be observed, the results may be used to diagnose some of the details of the energetic particle distribution in the magnetosphere. The magnitude of the precipitated flux is a function of the trapped particle distribution. For example, for typical trapped electron distribution interacting with a 5 kHz wave of 1 pT intensity at L = 4 the peak precipitated energy flux is found to be 5×10^{-3} ergs/cm^2 s. The predicted fluxes for typical parameters are 10^2-10^3 times larger than typical background precipitation levels at these latitudes and would be detectable with presently available instruments.

1. Introduction

The purpose of this paper is to study the precipitation of energetic electrons into the ionosphere due to the interaction of these particles with short-duration VLF waves in the magnetosphere. The time variation of the induced flux is computed for various wave frequencies, L values, pulse durations, and trapped energetic particle distribution functions.

Precipitation of the radiation belt particles is but one result of the gyroresonance interactions in the magnetosphere between energetic particles and whistler-mode waves. The waves involved in these interactions are (1) natural whistlers and chorus emissions, and (2) signals from ground-based sources, such as VLF transmitters and large-scale power grids, and emissions triggered by these signals. An important goal of the ongoing VLF wave-injection experiments carried out with the Siple Station VLF transmitter in the Antarctic [Helliwell and Katsufrakis, 1974] is to learn

how to control and precipitate the energetic particles by injected waves. These experiments and others have been highly successful in identifying the complex response of the magnetosphere to the injection of coherent VLF signals [Helliwell, 1974; Carpenter and Miller, 1976; Inan et al., 1977; Helliwell, 1977; Raghuram et al., 1977; Helliwell and Katsufrakis, 1978; Dowden et al., 1978; Chang and Helliwell, 1979; Helliwell et al., 1980b; Bell et al., 1981; Park, 1981; Tsuruda et al., 1982]. Particle precipitation induced by natural VLF/ULF waves (whistlers, chorus emissions, noise bursts) has been observed on numerous occasions [Rosenberg et al., 1971a; Helliwell et al., 1973; Helliwell et al., 1980a; Mende et al., 1980; Rosenberg et al., 1981; Dingle and Carpenter, 1981]. While direct correlation between manmade waves and precipitated particles has not yet been observed, there is evidence that observed narrow peaks in the energy spectra of precipitating electrons are due to interactions with VLF transmitter signals [Koons et al., 1981; Imhof et al., 1981]. Work is currently underway on detecting precipitation induced by manmade VLF waves: this work includes particle detectors on the Dynamics Explorer satellites [Hoffman, 1981]; HF ionosonde measurements of precipitation-induced density enhancements at Siple, South Pole, and Roberval Stations; photometer, riometer, and micropulsation measurements at Siple and/or Roberval Stations; and particle measurements on the SEEP satellite [Lockheed Report, 1979]. The results presented in this paper should provide a theoretical basis for these experiments.

For our analysis, we have employed an extension of a previous test particle simulation of the cyclotron resonance wave-particle interaction in the magnetosphere [Inan et al., 1978], wherein the wave-induced perturbations of the particle population are calculated by computing the full nonlinear trajectories of a large number of test particles in an inhomogeneous magnetosphere. Much of the background and justification for the approach used was given by Inan et al. [1978] and will not be repeated here. Relevant references for past work on scattering include Dungey [1963, 1964], Kennel and Petschek [1966], Roberts [1966, 1968, 1969], Gendrin [1968, 1974], Kennel [1969], Das [1971], Ashour-Abdalla [1972], Schulz and Lanzerotti [1973], Imhof et al. [1974], Lyons [1973, 1974a,b], and Vampola and Kuck [1978]. It suffices to point out that the approach used is required for simulating the particle perturbations induced by a coherent wave, which are fundamentally different from those produced by incoherent signals such as plasmaspheric hiss. In the latter case the particles execute a random walk in the velocity space [Roberts, 1966], whereas in the former the individual particles can undergo large pitch angle changes by resonating with the coherent wave over distances of many hundred wavelengths [Inan et al., 1978].

While the previously reported work considered

the steady-state case of the interaction of a
continuous VLF wave (CW) with the particle dis-
tribution, our present work deals with the temp-
oral variation of the flux precipitated as a re-
sult of the interaction of short-duration VLF
waves with the particles. During its propagation
between the two hemispheres the VLF wave pulse
interacts with particles of different energy and
pitch angle as determined by the gyroresonance
condition given below. The precipitated flux
thus consists of particles that have encountered
and interacted with the wave at different loca-
tions along the field line and that therefore
arrive at the ionosphere at different times. Our
computations take into account not only the full
nonlinear interaction of all test particles with
the wave but also account for the wave group
travel time and the particle travel times. The
results are given as precipitated energy flux as
a function of time after the injection of the
wave into the magnetosphere. The energy of the
downcoming particles is also given as a function
of time since this determines the ionospheric
altitude at which the flux is deposited [Rees,
1963; Walt et al., 1969; Banks et al., 1974] and
is therefore important for assessing the detect-
ability of the computed fluxes by using ground-
based instruments.

2. Physics of the Interaction

2.1 The Wave Structure

We consider a VLF wave pulse of finite dura-
tion injected into the magnetosphere at time
t=0. The pulse duration considered is typically
10-1000 wave periods, so that the pulse can be
treated as an approximately monochromatic signal.
The energy is assumed to propagate in a whistler-
mode duct in the magnetosphere as a circularly
polarized wave with the vector $\bar{k} \| \bar{B}_0$, where $\bar{B}_0$
is the static magnetic field. In the slowly
varying magnetospheric medium the wave magnetic
field intensity changes due to the changing re-
fractive index. Also for ducted wave propagation,
as is assumed here, the cross-sectional area of
the duct varies along the field line, being in-
versely proportional to the static magnetic field
intensity. If the whistler mode wave is assumed
to be the superposition of a large number of rays
that fill up the duct, then the intensity of the
VLF wave will also vary as the duct cross-section
changes. Both of these effects are taken into
account in our formulation. The wave magnetic
field can thus be expressed as

$$\bar{B}_w = B_{weq}(\omega_H k/\omega_{Heq} k_{eq})^{\frac{1}{2}}[\bar{a}_x \cos(\omega t -$$

$$\int_0^z kdz) + \bar{a}_y \sin(\omega t - \int_0^z kdz)] \qquad (1)$$

where z is the coordinate along $\bar{B}_0$, ω is the an-
gular frequency, k is the wave number, and $\bar{a}_x$
and $\bar{a}_y$ are the unit vectors in the x and y direc-
tions, and B_{weq}, ω_{Heq} and k_{eq} represent equator-
ial values. For whistler mode propagation along
the static magnetic field in a cold magnetoplasma,
k is given approximately by

$$k = (\omega_p/c)[\omega/(\omega_H - \omega)]^{\frac{1}{2}} \qquad (2)$$

where c is the speed of light, ω_p is the electron
plasma frequency, and ω_H is the electron gyro-
frequency. In this expression it has been as-
sumed that $(\omega_p/\omega_H)^2 \gg 1$.

For the background magnetoplasma, we have con-
sidered the case of a centered dipole model of
the earth's magnetic field and for most of our
calculations a diffusive equilibrium model of
the cold plasma distribution. A collisionless
model for the cold plasma distribution is used
for the results shown in Figure 19.

For our calculations of the particle scatter-
ing, we have not directly included the effects
on the wave of the electromagnetic fields gener-
ated by the perturbed particles. This amounts
to assuming either that the currents stimulated
in the energetic particle population do not lead
to significant damping or amplification of the
wave or that this effect has been included in
the model chosen for the wave structure. We
assume, in other words, that the wave field is
known as a function of space and time. Justifi-
cation for this assumption for the purpose of
computing the precipitated flux is given in ear-
lier work [Inan et al., 1978; Bell and Inan, 19-
81]. Experimental and theoretical evidence sug-
gest that the region of temporal growth is with-
in a few degrees of the geomagnetic equator [Hel-
liwell, 1967; Helliwell and Katsufrakis, 1974;
Tsurutani and Smith, 1974]. Any change in the
wave amplitude structure will thus occur over
a relatively small portion of the field line.
The effect of such a nonuniform amplitude varia-
tion on the total precipitated flux will be neg-
ligible. This point is further discussed in the
summary and conclusions section.

In comparing the precipitated fluxes for waves
at different frequencies we have assumed that
each wave is injected into the magnetosphere at
1000-km altitude with the same power level. Since
the medium is dispersive, this results in differ-
ent wave intensities at the equator for different
frequencies. For the case of propagation with
$\bar{k} \| \bar{B}_0$, the relation between the local power
density P and wave intensity is

$$B_w = (\mu \mu_0/c)^{\frac{1}{2}} P^{\frac{1}{2}} \qquad (3)$$

where μ is the refractive index and μ_0 is the
magnetic permeability of free space.

2.2. The Energetic Particle Distribution

The energetic particle population in the flux
tube is represented by an equatorial distribu-
tion function $f(v,\alpha)$, where v and α are equator-
ial values. In a dipole field the distribution
of particles at any other point along the field
line can easily be inferred from this [Roederer,
1970]. We assume that the initial distribution
of particles that interact with the wave remains
the same as the wave travels between the two
hemispheres. This should be a good assumption,
since the particles that resonante with the
whistler mode wave travel in the opposing direc-
tion; those that are perturbed by the wave do not
come back to the equator before a time equal to
their bounce period.

The initial unperturbed particle distribution
is taken to be of the form

$$f(v,\alpha) = \begin{cases} Av^{-n}g(\alpha) & \alpha \geq \alpha^{lc} \\ 0 & \alpha \leq \alpha^{lc} \end{cases} \qquad (4)$$

where A is a constant, n is an exponent that can be adjusted to produce agreement with observed distributions, $g(\alpha)$ is some function of pitch angle as may be required for anisotropic distributions, and α^{lc} is the angular halfwidth of the loss cone. The equatorial distribution function can also be written in terms of the differential energy spectrum at a given energy pitch angle, thus making comparisons with observed distributions easier. Thus for $\alpha \geq \alpha^{lc}$

$$f(v,\alpha) = \frac{m^2}{2E}\left[\frac{2E}{m}\right]^{n/2} \Phi_E v^{-n} g(\alpha) \qquad (5)$$

where Φ_E is the differential energy spectrum in el/cm^2 s sr keV of electrons with energy E (keV) and pitch angle $\alpha = 90°$, and m is the rest mass of the electron. The full distribution of particles is simulated in our model by a large number of test particles. Once the trajectories of the test particles in the wave are computed, the perturbed distribution is obtained. The calculation of the precipitated energy flux from the perturbed distribution is carried out in the same way as reported by Inan et al. [1978]. This procedure basically involves the integration of the quantity $\frac{1}{2} mv^2 v_{\shortparallel} f(v,\alpha)$ over energy and pitch angle within the loss cone.

2.3. The Wave-Particle Interaction

The gyroresonant interaction between the wave and the particles is depicted in the upper left panel of Figure 1. The wave is injected into the medium at 1000-km altitude at t=0. As it propagates up the field line it interacts with particles for which the resonance condition

$$\omega - \overline{k} \cdot \overline{v} \simeq \omega_H \qquad (6)$$

is locally satisfied. Cumulative energy exchange between the wave and particle can occur only if (6) is satisfied for an extended time period.

Since ω_H must exceed ω for the whistler mode, (6) is satisfied for electrons that travel in a direction opposite to that of the wave. Hence a new distribution of particles continually enters the wave packet as time progresses. As an example at a time $\tau = \tau_1$, for the wave packet position shown, a distribution of particles in $v_{\shortparallel}$ and α encounter the wave front. This is depicted in the right-hand side panel of Figure 1. Of these particles only those corresponding to the shaded area are expected to contribute to the precipitated flux. The α_{min} is determined by the loss cone, whereas α_{max} is determined by the maximum individual particle scattering for the given wave and at that point. The $v_{\shortparallel min}$ and $v_{\shortparallel max}$ are determined by the equatorial parallel velocity of particles that would go through a resonance with the wave at some time after $\tau = \tau_1$. These then are dependent on the position of the wave front, pulse duration (position of the wave tail), group velocity, and the particle travel time. The shaded area shown in Figure 1 is automatically

determined by the computer program, based on an input criterion. Usually the criterion is that all test particles that would be scattered in pitch angle by more than a specified amount be considered. A typical value used below would be $\Delta\alpha > 0.1°$ scattering for a 5 pT wave intensity.

To simulate the interaction of this group of particles that encounter the wave front at $\tau = \tau_1$, we represent the population in each mesh point with a number of test particles distributed in Larmor phase. Details of such representation and justification are given in the work of Inan et al. [1978]. The test particles are then input to the wave packet at $\tau = \tau_1$, with initial pitch angle of $\alpha°$ and parallel velocity of $v_{\shortparallel}$. The effect of the wave on the particle motion is given by the Lorentz force equation
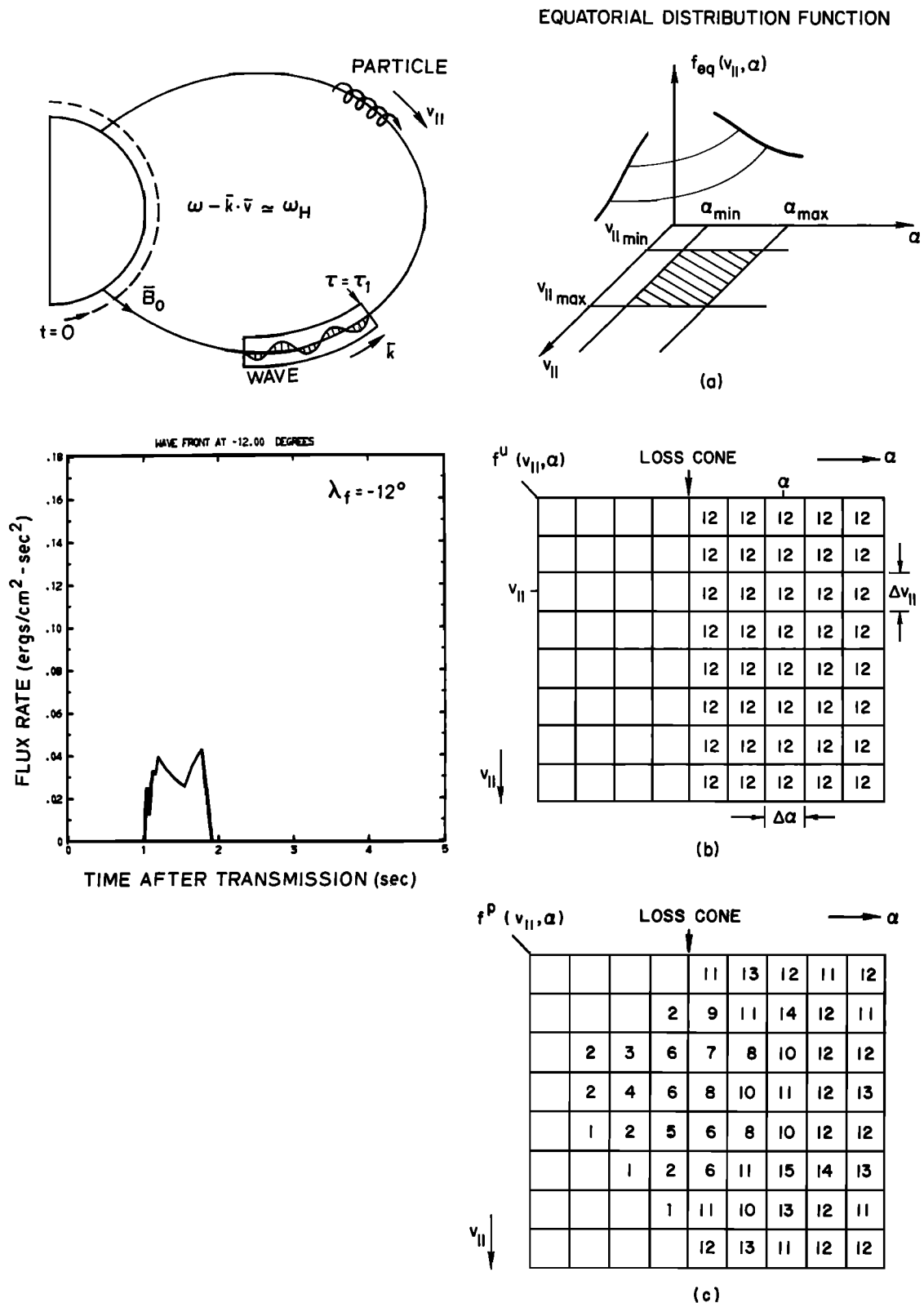
$$d\overline{v}/dt = -(e/m)[\overline{E}_w + \overline{v} \times (\overline{B}_w + \overline{B}_0)] \qquad (7)$$

where $\overline{v} = \overline{v}_{\shortparallel} + \overline{v}_\perp$ is the total velocity of the particle. A component form of this equation of motion has been given by previous authors [Dysthe, 1971, and others] and is not repeated here. The equations used in our simulation are identical to those used by Inan et al. [1978].

The equations of motion are integrated for each test particle until either the time when the particle exits from the wave tail or the time when the particle moves away from gyroresonance enough so that the wave perturbations become negligible. After this computation, the perturbed distribution function is obtained. The electrons that are scattered into the loss cone have a range of parallel velocities. Consequently, they are precipitated at the upper ionosphere (1000-km altitude) at different times, at which the energy flux per unit time can be obtained. The result is the rate of energy flux per unit time versus time, as shown in the lower left panel of Figure 1. Note that this flux is that due only to those particles (a full distribution in $v_{\shortparallel}$ and α) that meet the wave front at $\tau = \tau_1$ ± $\frac{1}{2}d\tau$. (Such a response constitutes an 'impulsive response' of the system, where the term 'impulse' in this context refers to the time of encounter of the particles and the wave front.) In the next $d\tau$ interval (corresponding to the next position of the wave front) another full distribution of particles will encounter the wave front, their responses will be slightly different since the interaction conditions are a function of latitude. Since by assumption the energetic particle motions do not affect one another, the interaction of each of these groups of particles can be separately calculated. The resulting responses can then be summed to give the total precipitated flux as a function of time.

2.4. Computation of the Precipitated Flux Versus Time

The energy flux response corresponding to each new position of the wave front (or at each time step) will be different due to the inhomogeneity of the medium. Since the cold plasma density and the static magnetic field intensity both change along the field line, the energy and pitch angle range of the near-resonant particles varies as well as the strength of the wave-particle interaction [Inan et al., 1978]. As a result of

EQUATORIAL DISTRIBUTION FUNCTION

PARTICLE

$v_{||}$

$\omega - \bar{k}\cdot\bar{v} \simeq \omega_H$

$f_{eq}(v_{||},\alpha)$

α_{min} α_{max}

$v_{||\,min}$

α

$v_{||\,max}$

$\bar{B}_0$

$\tau = \tau_1$

$\bar{k}$

$t = 0$

$v_{||}$

WAVE

(a)

WAVE FRONT AT -12.00 DEGREES

$\lambda_f = -12°$

FLUX RATE (ergs/cm^2-sec^2)

.18
.16
.14
.12
.10
.08
.06
.04
.02
0

0   1   2   3   4   5

TIME AFTER TRANSMISSION (sec)

$f^U(v_{||},\alpha)$ LOSS CONE   ⟶ α

α

$v_{||}$

				12	12	12	12	12
				12	12	12	12	12
				12	12	12	12	12
				12	12	12	12	12
				12	12	12	12	12
				12	12	12	12	12
				12	12	12	12	12
				12	12	12	12	12

$\Delta v_{||}$

$v_{||}$

⟶ $\Delta\alpha$ ⟵

(b)

$f^P(v_{||},\alpha)$ LOSS CONE   ⟶ α

				11	13	12	11	12
			2	9	11	14	12	11
	2	3	6	7	8	10	12	12
	2	4	6	8	10	11	12	13
	1	2	5	6	8	10	12	12
		1	2	6	11	15	14	13
			1	11	10	13	12	11
				12	13	11	12	12

$v_{||}$

(c)

Fig. 1. Schematics describing the wave-particle interaction and the calculation of the individual responses. The response $h(t,\tau_1)$ shown is caused by the particles that encounter the wave front at $\tau = \tau_1$. Note that a large number of such particles with different equatorial parallel velocities, pitch angle, and Larmor phase are considered. That is, each such response is computed by computing the perturbations of a full distribution of test particles. The width of the response is determined by the range of parallel velocities that corresponds to precipitated particles, the arrival time depends on the wave group velocity, and the particle travel time.

these, the effective pulse length (i.e., inter-
action length) seen by each particle is also dif-
ferent and must be taken into account. We express
this response as $h[t,\tau(\lambda_f)]$, where λ_f is the geo-
magnetic latitude of the wave front and is rela-
ted to the time τ by

$$\tau(\lambda_f) = \int_{-\lambda_1}^{\lambda_f} \frac{ds}{v_g \frac{d\lambda}{d\lambda}} d\lambda \qquad (8)$$

where s is the distance along the field line,
$v_g(\lambda)$ is the local group velocity of the whistler
mode wave, and λ_1 is the latitude at 1000 km al-
titude.

Figure 2 illustrates the variation of the res-
ponses $h(t,\tau)$ as a function of time τ (or λ_f).
The top panel shows the response due to the par-
ticles that encounter the wave at $-12°$ latitude
at time $\tau = \tau_1$. The precipitated electrons ar-
rive at the 1000-km ionospheric altitude at t =
1-2 s after the injection of the wave at the
same point. The middle panel shows the response
due to particles that encounter the wave front
at the equator, i.e., $0°$ latitude. The particles
arrive at the ionosphere at t = 3.3-3.7 s, indi-
cating that the range of parallel velocities of
particles that enter the wave at $\tau = \tau_2$ (and are
able to resonate with it) is narrower. This re-
sult is due to the fact that the variation of the
cold plasma parameters and hence that of the cy-
clotron resonant velocity of electrons in the
magnetosphere becomes smoother for lower latitudes
[Inan et al., 1978]. The lower panel shows the
response due to particles that encounter the
wave front at $+12°$ latitude and at a later time
$\tau = \tau_3$. The precipitated particles reach the
ionosphere at t = 3.2-4.2 s after transmission of
the wave. The range of parallel velocities in-
volved in this case and the one in the middle
panel are about the same. This response overlaps
in time with the response from $\lambda_f = 0°$ (middle
panel). An effect similar to this 'arrival time
convergence' effect has been previously reported
[Helliwell et al., 1980a] and can be roughly
described by using approximate analytical expres-
sions for wave group velocity and the unperturbed
parallel velocity of the resonant particles [Doo-
little, 1982]. It results from the fact that the
near-resonant electrons interacting with the wave
at higher latitudes beyond the equator are at a
higher energy and therefore can overtake the
lower-energy electrons that are near-resonant at
lower latitudes.

In our formulation we first compute the respon-
ses corresponding to a number of latitudinal po-
sitions of the wave front. (The number of steps
is chosen empirically as a function of the L
value and pulse length. As an example, for L =
4 and a 400-m s wave pulse, latitudinal steps
separated by $4°$ were taken. The criteria used
were to make the latitude steps comparable to
the spatial length of the pulse at the equator.)
Since the medium is slowly-varying, the responses
due to the in-between wave front positions can
then be calculated by using linear interpolation.
The total response, i.e., the total precipitated
energy flux as a function of time, is then the

sum of the contributions at each time from all of
the different responses. In other words,

$$r(t) = \int_0^{\infty} h(t,\tau) d\tau \qquad (9)$$

where r(t) is the precipitated energy flux at
1000-km altitude as a function of time after the
transmission of the wave at the same point.

A typical energy flux versus time curve, com-
puted as described, is given in the top panel of
Figure 3. Flux in ergs/cm^2 s is shown as a func-
tion of time after transmission for a 0.4-s long
pulse of 5 pT intensity at a frequency of f = 6.83
kHz propagating along the L = 4 magnetic field
line. The wave frequency in this case is one-
half the minimum gyrofrequency along the field
line. The result given is for a diffusive equi-
librium model and an equatorial cold plasma den-
sity n_{eq} = 400 el/cc corresponding to a plasma
frequency of f = 180 kHz. The energetic particle
distribution is given by (4) or (5) with $g(\alpha)$ = 1
(isotropic), n = 6, and Φ_E = 10^8 el/cm^2 s sr keV
for E = 1 keV.

The geomagnetic latitude of the wave front (t_f)
and tail (t_t) as a function of time is shown in
Figure 4. The solid portions of these curves are
the positions for which computations were carried
out. The dotted portions show the times for which
the wave-induced scatterings are negligible. The
spatial extent of the pulse at any time is the
vertical separation between the t_f and t_t curves.
Note that the spatial pulse length is a minimum
around the equator. Also shown on the same fig-
ure is the maximum and minimum arrival time of
the precipitated particles. The latter is shown
for each of the wave front latitudinal positions
for which an impulse response was computed. The
information in this figure can be used to deter-
mine the range of interaction latitudes that con-
tribute to the flux at different times.

The increase in the flux after approximately
t = 2.5 s is due to the arrival time convergence
effect mentioned above. The exact shape of this
curve depends on the wave pulse length, frequency,
and the particle distribution function, as will
be shown below.

The lower panel in Figure 3 gives the energy
range of the downcoming precipitated flux as a
function of time. We have plotted the energy
versus arrival time for each of the impulse re-
sponses used to compute r(t). In this case the
impulse responses were computed for wave front
positions λ_f of between $-20°$ to $+48°$ geomagnetic
latitude with steps of 4 degrees. At any time t,
the energy range of the precipitated particles
is thus defined by the curves given in Figure 3
(lower panel). For example, it can be seen that
the flux at t = 4 s consists of particles from
much narrower ranges of energies (0.4 keV-0.6
keV) than that at t = 3 s (0.4-5 keV).

3. Precipitated Flux Versus Time

In this section we discuss results obtained
by applying the formulation described above to
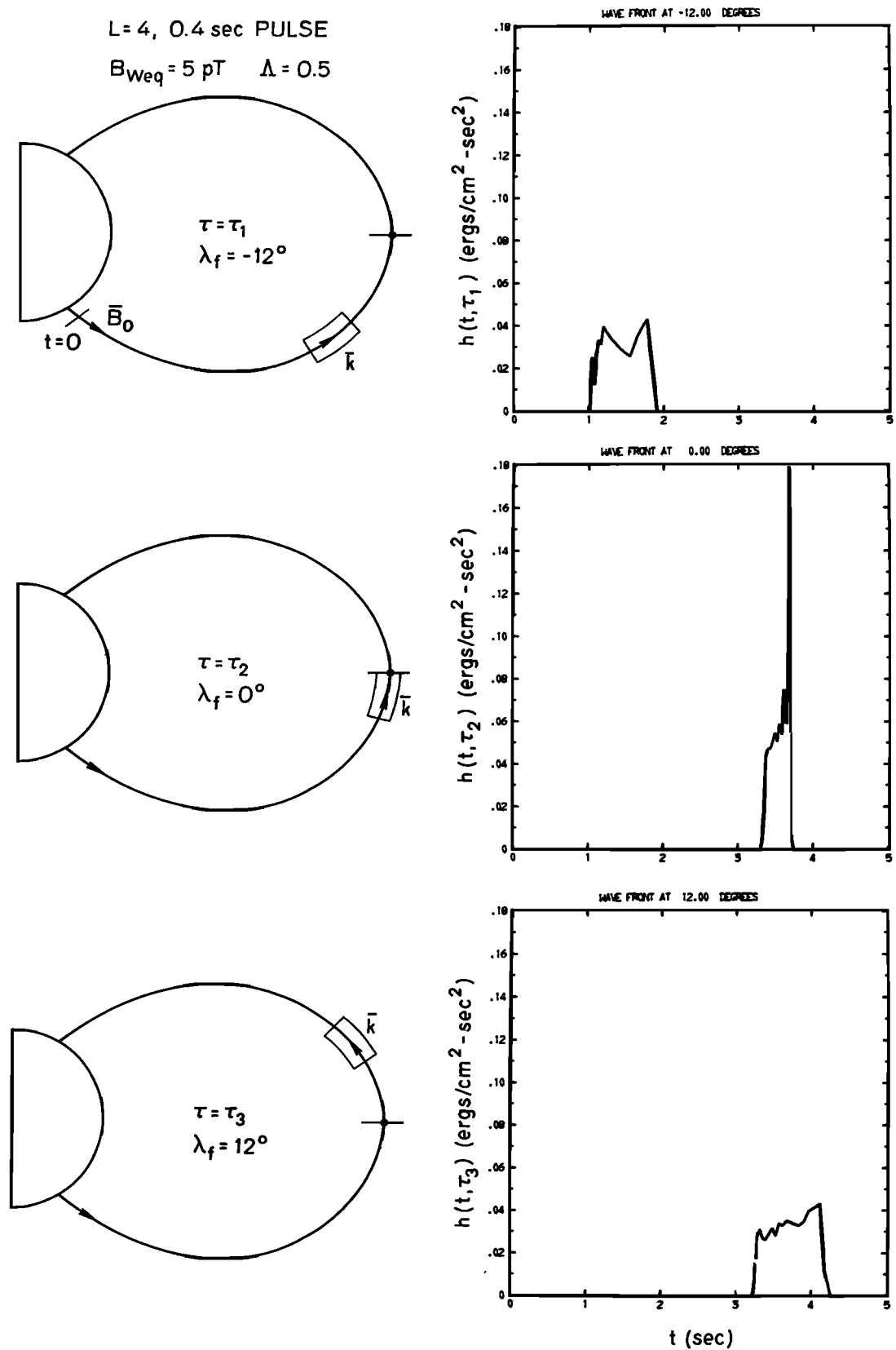various different magnetospheric conditions.

Fig. 2. The responses due to three different positions of the wave front as it propagates along the field line. The arrival time of the pulse for the bottom panel is comparable to the one above even though this response is due to those particles that meet the wave at a later time. This is due to the fact that the energies of the resonant particles are higher for the former case.

3.1. Dependence on Wave Pulse Length

Figure 5 shows the computed precipitated flux versus time due to wave pulses of 5 pT intensity (at the equator) and of different lengths PL at a normalized frequency $\Lambda = f/f_{Heq} = 0.5$ propagating along the L = 4 field line where the equatorial cold plasma density is taken to be $n_{eq} = 400$ el/cc. The energetic particle distribution function is assumed to be as given in (5) with $g(\alpha) = 1.0$ and n = 6. Wave pulse lengths of PL = 50 m s to 800 m s are considered. The energy ranges of the downcoming particles are shown in the right-hand column. It should be noted here that the number of latitudinal steps taken to

Fig. 4. The latitudinal position of the wave front (t_f) and tail (t_t) as a function of time is shown by the solid continuous curves. The dotted portion of these curves show the times for which the wave-induced scatterings are negligible. Thus the computations were limited to the regions corresponding to the solid lines. Also shown (t_e) is the maximum and minimum arrival time at 1000-km altitude of electrons that meet the wave front at different latitudes. Each segment here corresponds to a wave front position for which an impulse response is computed.

compute the impulse responses were taken to be inversely proportional to pulse length.

The duration of the precipitated pulse is in the 3-4 s range, determined mainly by the wave and particle travel times on this field line, as discussed in connection with Figure 4. The important feature shown in Figure 5 is the variation of peak flux level with wave pulse length. For PL > 200 ms, the peak flux begins to saturate. Further increases in pulse length result in broadening of the precipitation pulse in time and a widening of the range of particle energies that constitute the flux.

For PL < 200 ms the peak flux decreases with decreasing PL. This is partly explained by the fact that the effective pulse length seen by the near-resonant particles (= half the pulse length at the equator and for $\Lambda = 0.5$ for which case $v_g = v_{||}$) becomes less than the interaction length (the 'interaction length' in this context is defined as the distance over which the particle parallel velocity stays within a few percent of the local resonance velocity.) allowed by the inhomogeneity of the medium [Inan et al., 1978]. This result implies that if controlled precipitation can be achieved, then the variation of the peak precipitated flux with PL can be used to diagnose the parameters that control this interaction length. Some of these parameters are the wave intensity, cold plasma density, and the latitudinal location of the interaction region [Inan et al., 1978; Bell and Inan, 1981].

Partly contributing to the decrease in the flux for PL $\leq$ 200 m s is the diminishing of the arrival time convergence effect, evident in a reduction of overlap of the energy-versus-time curve segments.

We have discussed the arrival time convergence effect that causes the increase in flux for t = 3-4 s in connection with Figure 3. From the top right panel of Figure 5 we see that there also exists some convergence effect at t = 2.5-3.5 s

TIME AFTER TRANSMISSION (sec)

Fig. 3. The top panel shows the precipitated energy flux versus time after injection of the wave into the magnetosphere at 1000-km altitude. The bottom panel shows the energy of the particles that constitute the flux. Each separate segment shows the energy versus arrival time for one of the responses corresponding to one of the positions of the wave front. In this case the individual responses were computed for $\lambda_f = 16°$ to 44° with steps of 4°.
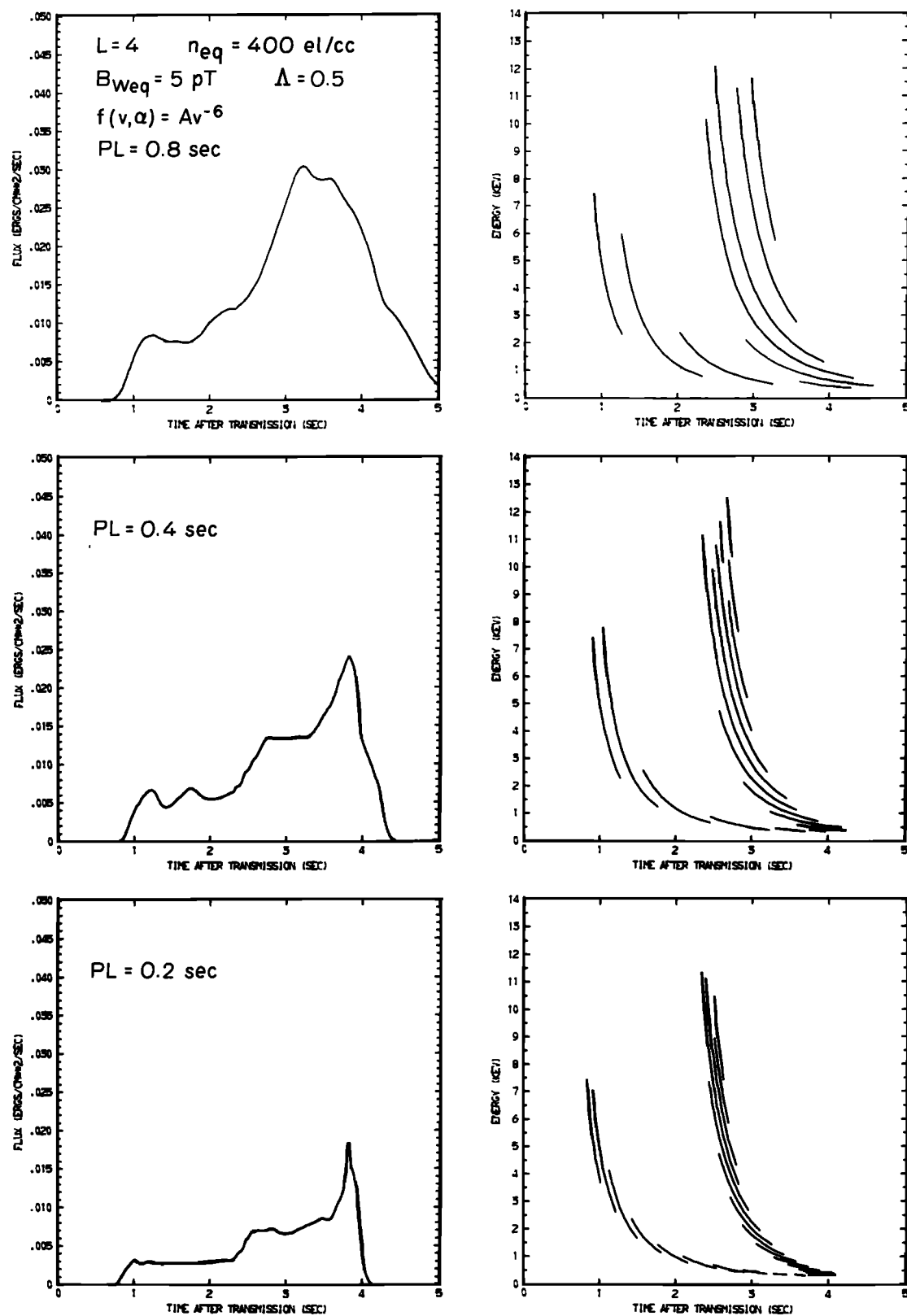
Fig. 5.   Precipitated energy flux versus time and energy versus time curves for differ-
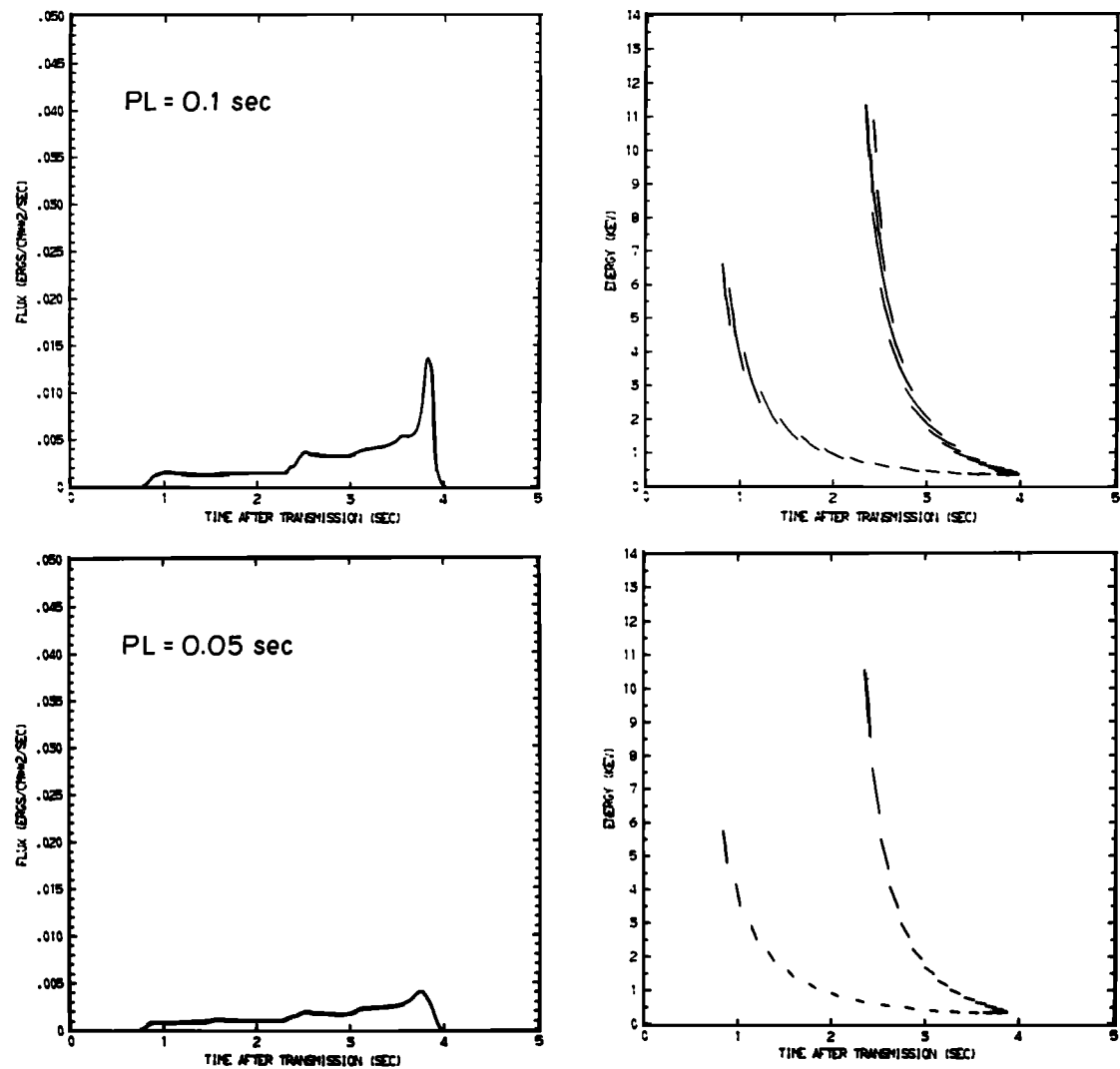ent wave pulse lengths PL.

Fig. 5. (continued)

for the case of PL - 800 m s. This is also evident from the broadening of the peak in the flux versus time curve around the same time. This effect can be understood by noting that at any fixed time the 800 m s pulse occupies at least a 32° latitude range along a field line. Thus the wave tail can be interacting with higher-energy particles that resonate to the south of the magnetic equator (which therefore arrive around 2-3 s) even when the wave front is well above the equator. This effect is also visible, albeit to a lesser extent, for the 400 m s pulse.

Figure 6 shows the integrated energy density in ergs/cm^2 as a function of pulse length. It is evident that this quantity increases with pulse length even though the peak flux remains more or less constant. This result is expected, since the longer pulses represent more wave energy.

3.2. Dependence of Normalized Frequency

The results shown in Figure 5 are for a normalized frequency of $\Lambda = 0.5$. In Figure 7 we show the computed precipitated flux versus time for PL = 400 m s and for $\Lambda = 0.05$, 0.1, 0.25, 0.5,
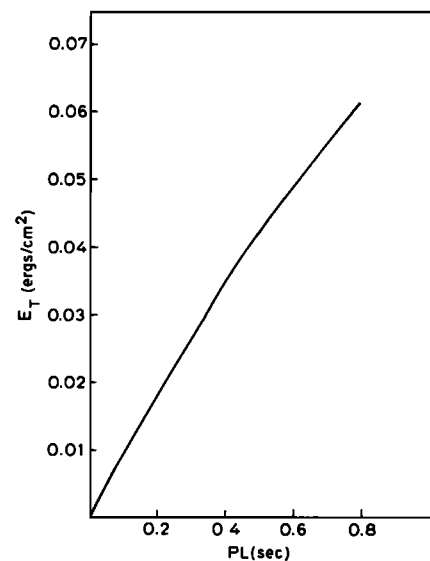
Fig. 6. Total deposited energy as a function of PL, for the cases shown in Figure 5.
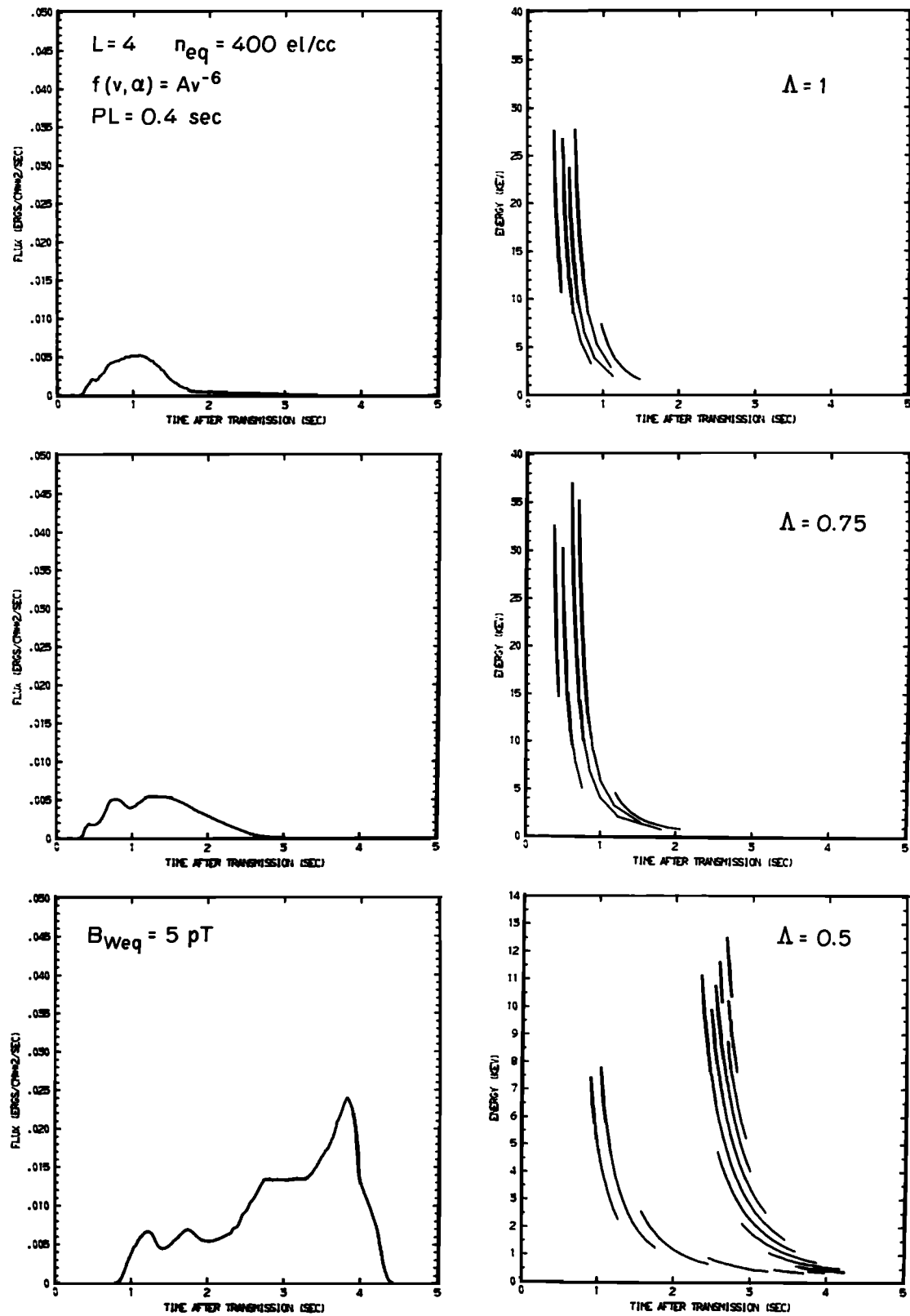
Fig. 7. Precipitated energy flux and particle energy versus time for different normalized frequencies Λ.
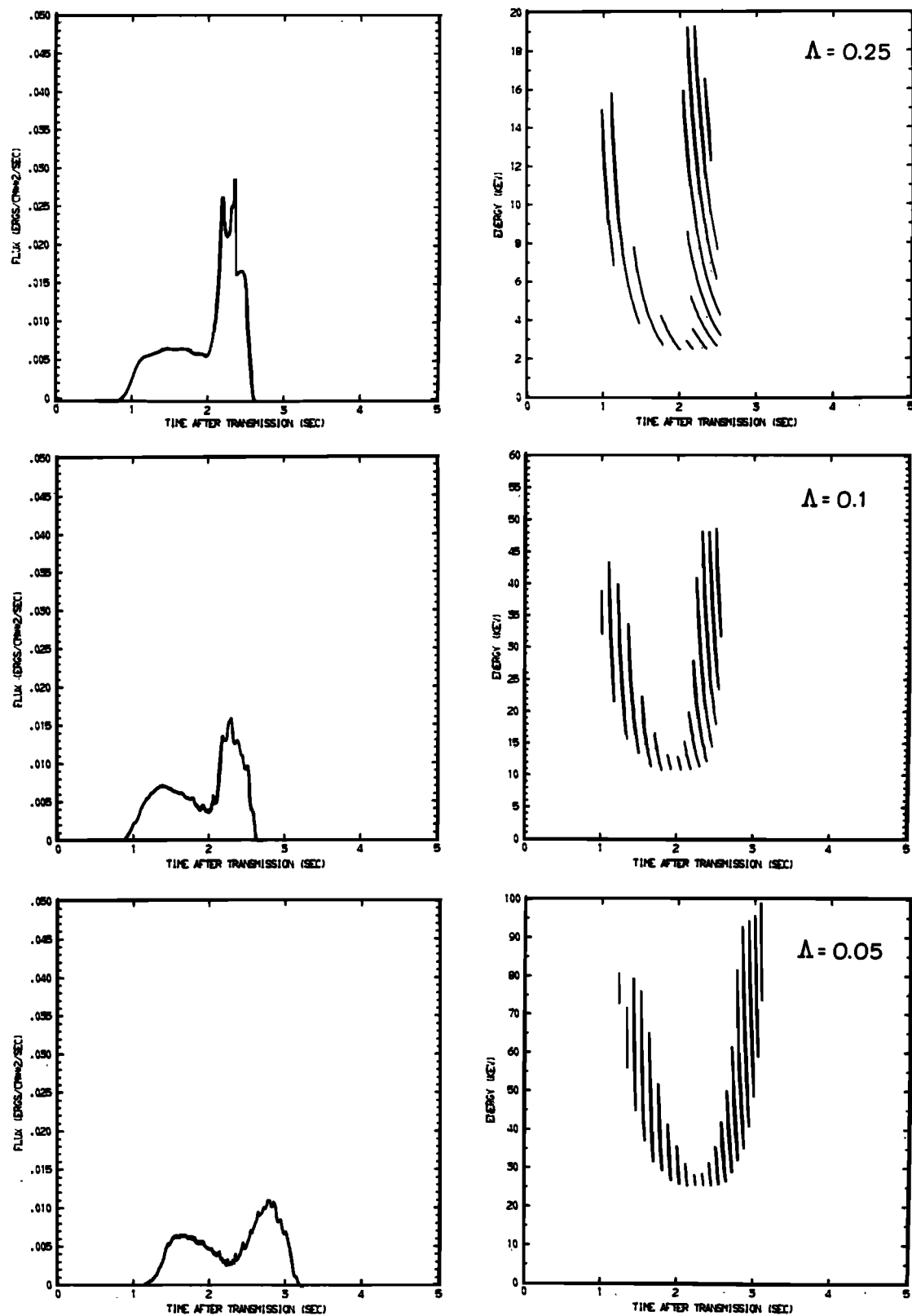
Fig. 7. (continued)

0.75, and 1.0, while the other parameters are kept the same as in Figure 5. Since we have limited our formulation to waves that propagate in whistler mode ducts of enhanced ionization [Smith et al., 1960], propagation over the magnetic equator is only possible for frequencies $\Lambda < 0.5$ [Helliwell, 1965]. For $\Lambda > 0.5$, the ray paths will deviate from the magnetic field line at the point where the wave frequency becomes equal to one-half the local electron gyrofrequency. Although propagation with $\Lambda > 0.5$ is possible in depletion ducts [Inan and Bell, 1977], we limit our discussion to the more common case of whistler mode propagation in enhancement ducts. Thus in our simulation of the wave-particle interaction for the waves with $\Lambda > 0.5$, we have terminated the interaction when the wave tail crosses the point where $f = 0.5 f_H$.

In comparing results for different normalized frequencies, the input wave power at 1000-km altitude is kept constant, as discussed in connection with (3). This results in different wave intensities at the equator that can be computed by using (1) and (3) and a model of the distribution of the cold plasma along the field line. Figure 8 shows the wave intensities at 1000-km altitude and at the equator for the case of a diffusive equilibrium model of the plasma [Angerami and Thomas, 1964]. The equatorial intensities are not given for $\Lambda > 0.5$, since these waves do not reach the magnetic equator on that field line, as discussed in the preceding paragraph.

In the $\Lambda < 0.5$ cases (Figure 7), the length of the precipitation pulse is shorter for $\Lambda = 0.25$ and $\Lambda = 0.1$ than for $\Lambda = 0.5$. This could be due to the fact that (1) the wave group delay for different frequencies is different and (2) that the energies of the particles that resonate with lower-frequency waves are higher and the particles thus travel faster. For the $\Lambda = 0.25$ case, the group delay is not much different from that of the $\Lambda = 0.5$ case. Therefore the decreased duration of the precipitation pulse is mainly due to the second effect cited above. For the $\Lambda = 0.1$ case, although the group delay is larger, the second effect is large enough to make the precipitation pulse length shorter than for the $\Lambda = 0.5$ case and comparable with the $\Lambda = 0.25$ cases. We also note that the pulse length is longer for the $\Lambda = 0.05$ case, for which the wave group delay is much longer.

Next we discuss the magnitude of the flux for $\Lambda \leq 0.5$. As frequency is decreased, there are two imporant factors that will determine the flux: (1) the increased energy of the near-resonant particles result in shorter effective interaction lengths and thus less scattering [Inan et al, 1978], and (2) the energy flux is proportional to energy, and thus a given number of scattered particles at a higher energy corresponds to more energy flux. from Figure 7, the fact that the peak flux for the $\Lambda = 0.25$ case is somewhat higher than for $\Lambda = 0.5$ indicates that the second effect is more important at $\Lambda = 0.25$, whereas the results for $\Lambda = 0.1$ and 0.05 indicate that the first effect becomes dominant as frequency is further reduced.

The precipitation pulse changes into a double-peaked curve for $\Lambda = 0.1$ and 0.05. These results are a function of the energetic particle distribution function, namely n, in (5) above. The case shown in Figure 7 is for n = 6. The dependence

of the peak flux on n will be discussed further in the next section.

Another factor contributing to the reduced peak flux for the $\Lambda = 0.1$ and 0.05 cases is the fact that the arrival time convergence effect is reduced as a result of the increased energies of the near-resonant particles. This is evident from Figure 7, where we note that there is much less overlap between the arrival times of the particles that meet the wave front at different latitudes.

We now discuss the $\Lambda > 0.5$ cases that are shown in Figure 7. For reference, it should be noted that the points where locally $f = f_H/2$ for the $\Lambda = 0.75$ and 1.0 cases are geomagnetic latitudes $\lambda = 17°$ and $23°$, respectively. The wave-particle interaction is thus assumed to be terminated when the wave tail crosses these latitudes. Note here that since the wave pulse does not reach the magnetic equator on this field line, the shape of the precipitation pulse is different than those for $\Lambda < 0.5$. The smooth tail end of the precipitation pulse is due to the fact that after the wave front crosses the $f = f_H/2$ point, the effective pulse length (and thus the interaction length) seen by the particles continually decreases as the wave tail approaches the same point. There exists no sharp peaks since the arrival time convergence effect is not present. The maximum (peak) flux is lower than that for $\Lambda = 0.5$. Another reason for the decreased flux is the fact that the wave-particle interactions occur away from the equator, where the interaction lengths and thus the total particle scatterings are reduced to the increased inhomogeneity. [Inan et al., 1978]. For the results of Figure 7, the peak flux corresponds to the interactions with particles that enter the wave front closest to the local $f = f_H/2$ point. As frequency is further increased the peak flux continues to decrease, as would be expected.

The total integrated energy density for the cases shown in Figure 7 is given in Figure 9 for reference.
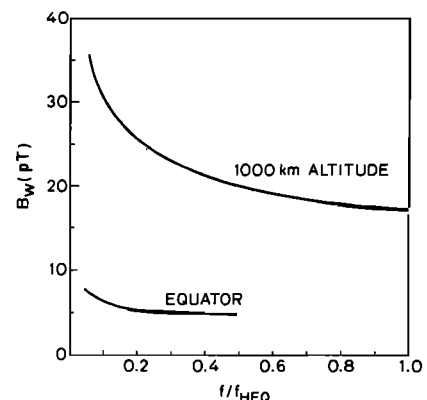

Fig. 8. Wave magnetic field intensity at 1000-km altitude and at the magnetic equator for a constant power input P at 1000-km altitude. This result is computed by using (3) and a diffusive equilibrium model of the cold plasma density. The power input is taken to be such that the wave intensity at the equator for L = 4, $n_{eq} = 400$ el/cc, and $\Lambda = 0.5$ is 5 pT. The variation of B_W with Λ is independent of L value. The equatorial intensities for $\Lambda > 0.5$ cases are not shown.

3.3. The Role of f(v,α)

The results shown in Figures 5 and 7 are for an energetic particle distribution function, as given in (5), with n = 6. In order to show the effect of the spectral composition of the trapped particle distribution on the precipitated flux, we show in Figure 10 precipitated flux versus time for n = 4, 6, and 8. For this we have used Λ = 0.5, PL = 400 m s, and B_w = 5 pT at L = 4 and n_{eq} = 400 el/cc. The differential energy spectrum for which the distribution in (5) is normalized was taken to be Φ_E = 10^8 el/cm^2 s sr keV for particles with 90° pitch angle at the equatorial resonant energy E = 0.372 keV rather than at 1 keV, as was the case for Figure 5. This renormalization is necessary in order to more clearly see the relative effects of the off-equatorial interactions as a function of n.

We observed from Figure 10 that for n = 4 the precipitation pulse is double-peaked (also note the difference in scale). This is due to the fact that the precipitated energy flux is proportional to v^{5-n} (as will be established in the following section) and that therefore for this case the flux due to electrons that resonate at higher latitudes (thus having higher energy) is larger than that from the ones that resonate at the equator. Consequently, the wave pulse as it approaches the magnetic equator induces more precipitated energy flux, thus accounting for the early peak around t = 1.0 s after transmission. As n increases the available number of high-energy particles decreases and this effect disappears as expected. Also note that as n increases above 6 the value of the peak flux at t = 3.8 s also decreases, since this peak is due to the superposition of particles that have interacted with the wave front at latitudes above the equator. This is evident from the energy versus time curve given in Figure 7 for Λ = 0.5, which corresponds to the case in Figure 10. Note that this curve is independent of n, since it shows the energies that have a finite contribution to the flux at any given time.

The fact that the shape of the precipitation pulse depends on the energetic particle distribution can have important implications. If controlled precipitation of energetic particles from the magnetosphere can be achieved, this information can possibly be used as a diagnostic tool for ground-based studies of the details of
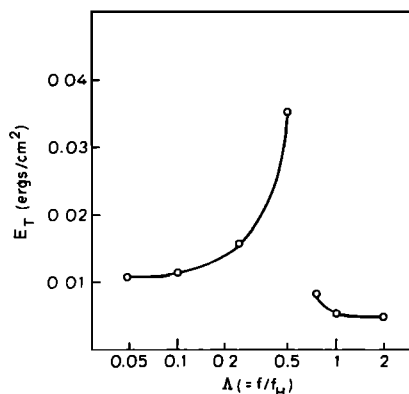

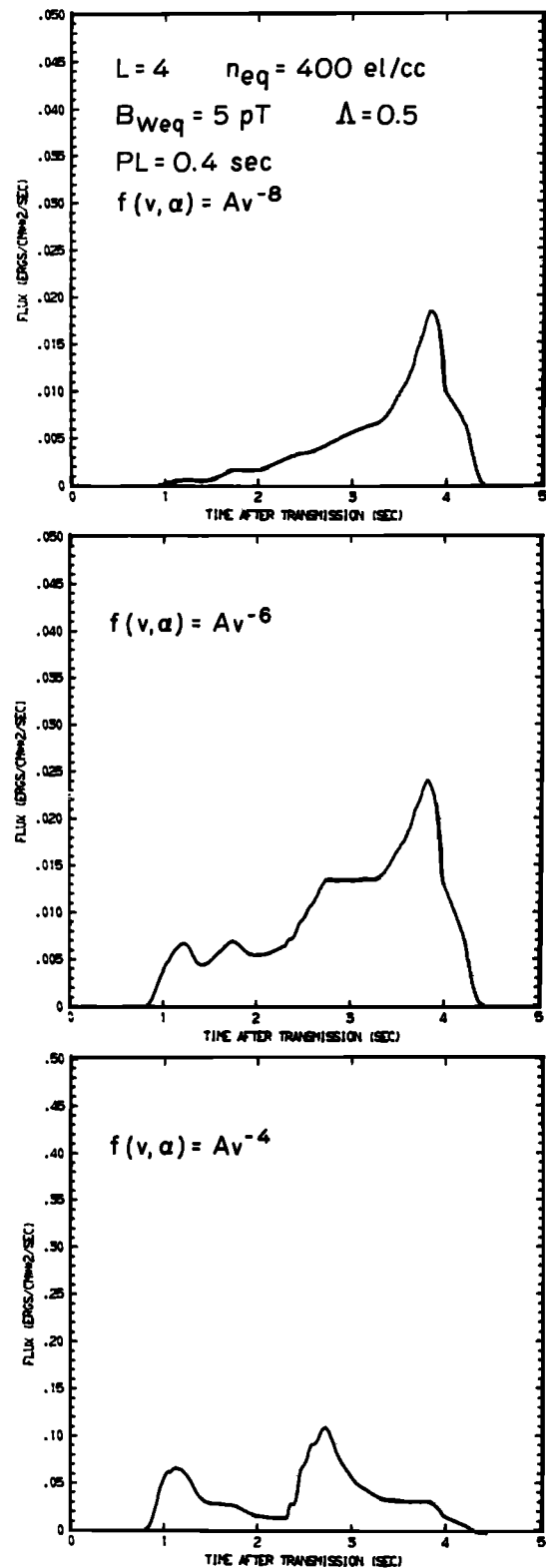Fig. 9. Total deposited energy versus Λ for the cases shown in Figure 7.

Fig. 10. Precipitated energy flux versus time for different values of the distribution function exponent n. Note that the vertical scale is different for the bottom panel. The energy versus time curves for all three cases is identical to that shown in Figure 3. The differential energy spectrum for these cases was taken to be Φ_E = 10^8 el/cm^2 s sr keV for electrons with E = 0.372 keV energy (equatorial resonant energy at L = 4 and n_{eq} = 400 el/cc).
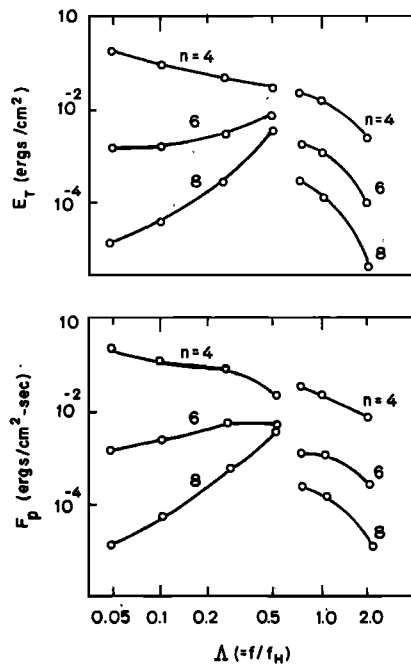
Fig. 11. Total deposited energy E_T and peak precipitation flux F_p as a function of Λ for three different values of n. All other parameters have the same value as in Figure 10.

the energetic particle distribution near the loss cone. It is also evident from Figure 10 that the total integrated energy density is also larger for smaller n, another factor that can possibly be useful in ground-based diagnostics.

Having established the parameters that control the temporal variation of the precipitated flux, we now focus our attention on a few parameters that approximately characterize the flux. These
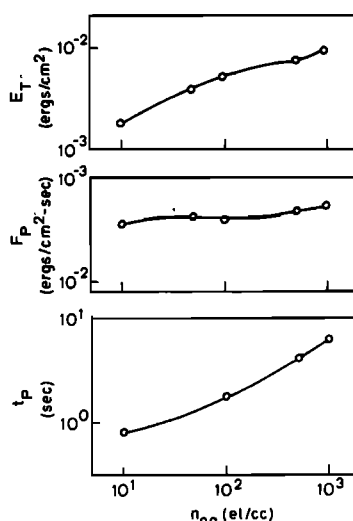
are (1) peak flux, (2) integrated energy density, and (3) occurrence time of the peak.

4. Peak Flux and Total Deposited Energy

The result shown in Figure 10 was for $\Lambda = 0.5$. Those given in Figure 11 demonstrate the role of the distribution function exponent at other frequencies. Here, we have not shown the details of the time variation of the fluxes; instead we have chosen two parameters that characterize the flux versus time curves similar to those of Figure 10. These are (1) the peak value of the flux F_p and (2) the integrated energy deposition (or total deposited energy) E_T (ergs/cm^2). The latter quantity conveys information on the 'equivalent width' of the precipitation pulse. Figure 11 shows these two quantities for normalized frequencies $\Lambda = 0.05$-2.0 and for wave intensity of $B_w = 1$ pT at the equator for $\Lambda \leq 0.5$ and at the $f = \frac{1}{2}f_H$ point for $\Lambda > 0.5$. All other parameters are the same as those of Figure 10. The curves for $\Lambda \leq 0.5$ and $\Lambda > 0.5$ are shown as separate segments since for the $\Lambda > 0.5$ case the wave does not reach the magnetic equator, resulting in an abrupt reduction in peak flux, as discussed in connection with Figure 7. The results of Figure 11 can be understood in light of the earlier discussions of Figures 7 and 10. For n = 4 and $\Lambda \leq 0.5$, both F_p and E_T increase with decreasing frequency, while they decrease for the case of n = 6 and 8. This indicates that the energy flux is proportional to approximately v^{5-n}. For $\Lambda > 0.5$, the resonant particle energy increases with frequency; however, both F_p and E_T continue to decrease for n = 4, 6, and 8. This arises from the fact that for $\Lambda > 0.5$ the peak interaction takes place further away from the equator for higher frequencies, resulting in less efficient interaction and less flux.
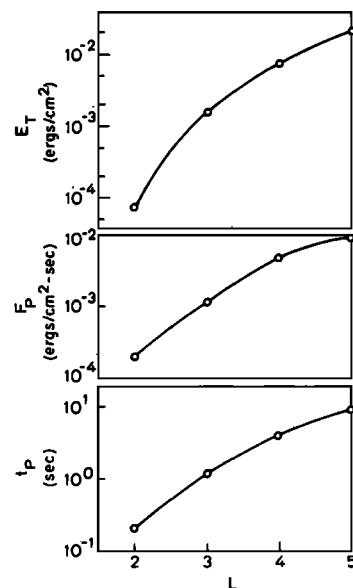

Fig. 12. Total deposited energy E_T, peak precipitation flux F_p, and the arrival time of the peak flux t_p as a function of n_{eq}. This result is computed for L = 4, $\Lambda = 0.5$, $B_w = 1$ pT (at the equator), n = 6, and $\Phi_E = 10^8$ el/cm^2 s sr keV for E = 1 keV.

Fig. 13. Total deposited energy E_T, peak precipitated flux F_p, and the arrival time of the peak flux t as a function of L value. This result is computed for $n_{eq} = 400$ el/cc, with all other parameter values being the same as in Figure 12.
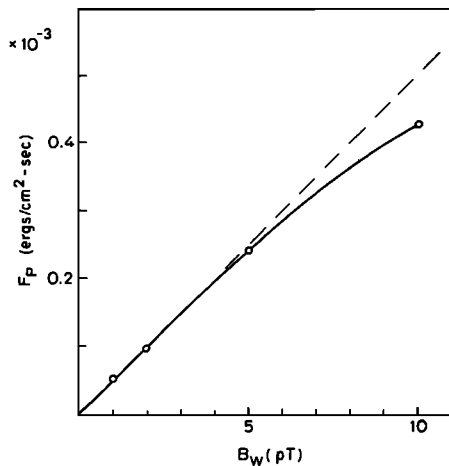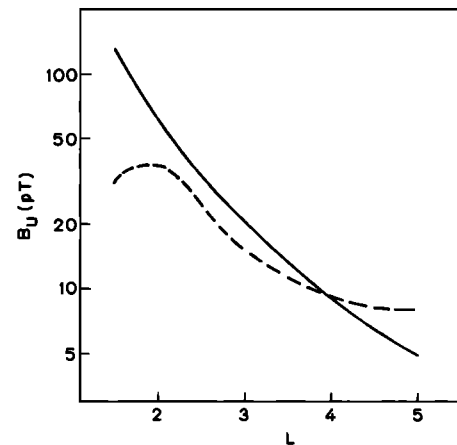
Fig. 14a.

Fig. 14b.

Fig. 14. (a) Peak precipitation flux F_p as a function of the wave intensity at the equator B_w. The result shown is for n_{eq} = 400 el/cc; all other parameter values being the same as in Figure 12. (b) Upper limit on the wave intensity B_u as a function of L value. B_u is computed by setting the parameter ρ = 1, where ρ is defined by Inan et al. [1978] and represents the ratio of the wave and inhomogeneity forces for equatorial interactions. The solid line shows B_u computed by assuming n_{eq} = 400 el/cc at all L values. The dotted line shows B_u, where n_{eq} is taken to be as given in Figure 16. B_u is proportional to $n_{eq}^{2/3}$.

4.1. Dependence on n_{eq} and L

Next we discuss the dependence on cold plasma density n_{eq}, which determines the resonant energy through (2) and (6). Figure 12 shows E_T, F_p, and the arrival time of the peak flux t_p as a function of n_{eq} at L = 4, for Λ = 0.5, B_w = 1 pT (at equator) and n = 6. The differential energy spectrum was taken to be Φ_E = 10^8 el/cm² s sr keV for particles with α = 90° and E = 1.0 keV. We have used a diffusive equilibrium model for the cold plasma density for all values of n_{eq}. This should be a good assumption in all cases except perhaps for n_{eq} = 10 el/cc; however, calculations with a collisionless model for this value have resulted in less than 10% difference, which is hardly noticeable on the scale shown. The results of Figure 12 can be understood by noting that the wave group velocity and the resonant particle velocity are proportional to $n_{eq}^{1/2}$. Hence the decrease with n_{eq} of the arrival time of the peak of the precipitation pulse is as expected. The decrease with n_{eq} in E_T indicates that the duration of the precipitation pulse decreases for the same reason. This is due to the combined effect of arrival time convergence, scattering efficiency, and the energy range of the particles that contribute to the peak.

We have up to now shown results for L = 4. In order to show the dependence on L value, we present in Figure 13 the computed variation of flux as a function of L. Here we have kept n_{eq} = 400 el/cc at all L values. All other parameters have the same values as those for Figure 12. We see that E_T, F_p, and t_p all decrease rapidly with decreasing L. This is due to the fact that the static magnetic field along a given field line changes more rapidly with distance at lower L values, thus resulting in decreased interaction lengths. The total deposited energy at

L = 2, for instance, is more than two orders of magnitude smaller than that at L = 5 for the same parameters.

4.2. Dependence on Wave Intensity

For parameter values similar to those used in this paper, it was demonstrated by Inan et al. [1978] that the root mean square scattering of individual particles at L = 4 was proportional to wave magnetic field intensity for B_w < 10 pT. To demonstrate the same in terms of the total and peak energy flux, we show in Figure 14a computed values F_p as a function of B_w. The result indicates that these quantities are linearly proportional to B_w for B_w < 10 pT, with the deviation from linearity at B_w = 10 pT being about 10%. This fact is useful in terms of the computations since it means that results of test particle simulations for a specific B_w can be scaled up or down to obtain the flux values at other values of B_w, as long as B_w < 10 pT. It should be noted that since the inhomogeneity factor is stronger at lower L values the range of B_w values for which linearity holds is wider [Inan et al., 1978]. This is shown in Figure 14b, where we plot the upper limit B_u on wave intensity, below which the flux is roughly proportional to B_w as a function of L value. The solid line shows B_u computed for n_{eq} = 400 el/cc, Λ = 0.5, and for a threshold of linearity defined as ρ = 1, where ρ is the ratio of the wave and inhomogeneity terms as defined in Inan et al. [1978]. It can be shown that B_u is proportional to $n_{eq}^{2/3}$. The dotted line shows B_u again for Λ = 0.5 and ρ = 1, but with n_{eq} varying with L shown in Figure 16.

In this paper and in the following figures we confine our attention to those cases where B_w < B_u. Note that this does not necessarily mean that individual particle trajectories are linear;
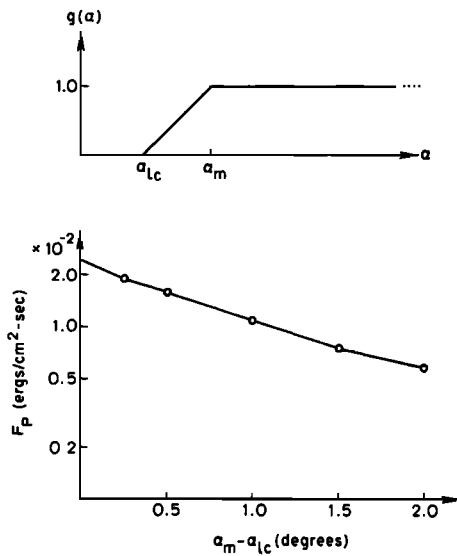
Fig. 15. Peak precipitated flux F_p as a function of the loss cone anisotropy.

this does indicate, however, that trapped particles constitute a small fraction of the total number of particles in the simulation. The trajectories of all test particles are accurately computed by solving the full equations of motion, regardless of their being trapped or nontrapped in the wave's potential well.

4.3. Effect of Anisotropy of f(v,α)

For most of the results presented in this paper we use an isotropic energetic particle distribution with $g(\alpha) = 1$ with an abrupt loss cone. For an anisotropic distribution peaked around $\alpha = 90°$, the precipitated flux values can be obtained from those given by simple scaling as long as $g(\alpha)$ is flat for a few degrees above the loss cone [Inan et al., 1978]. In this case the flux values would be reduced by a factor of $g(90°)/g(\alpha_{lc})$, where α_{lc} is the half-angle of the loss cone.

In cases of strong anisotropy in the vicinity of the loss cone, such scaling would not be valid. Figure 15a shows the vicinity of the loss cone where we have assumed a linear variation of $g(\alpha)$ with α. The parameter that defines this variation is $\alpha_m - \alpha_{lc}$, where is fixed. Figure 15b shows the computed peak flux as a function of this parameter. All other parameters are taken to be the same as those of Figure 3. The peak flux approaches the value of 2.5×10^{-2} ergs/cm² s as α_m goes to α_{lc}, i.e., $g(\alpha)$ approaching the abrupt variation used in the earlier results. The flux is reduced by an order of magnitude for $\alpha_m - \alpha_{lc} \simeq 4°$.

It should be noted that for most of the cases considered in this paper, including those at different L values, the precipitated flux is comprised of particles that have initial pitch angles within a few degrees of the loss cone. Thus behavior similar to that shown in Figure 15 can be expected over a wider range of the parameters.

5. A Case Study

Having established the dependence of precipitation on various parameters, in this section we

apply our formulation to a realistic magnetospheric case. We consider a diffusive equilibrium model of the cold plasma with an equatorial cold plasma density profile as shown in Figure 16, starting with 3000 el/cc at L = 1.5 and gradually decreasing to 400 el/cc at L = 4, the density value that was used in the above results. For L = 5, we have considered two cases: an inside-plasmapause case of n_{eq} = 200 el/cc (as shown in Figure 16) and an outside-plasmapause case of 10 el/cc. For the latter, we have used a collisionless model of the cold plasma density [Angerami, 1966].

The energetic particle distribution was taken to be the same at all L values, with $g(\alpha) = 1$, $\Phi_E = 10^8$ el/cm² s sr keV at E = 1 keV and $\alpha = 90°$ and n = 6. This does not necessarily represent a general case; however, since precipitated flux is proportional to Φ_E, results for any specific case can easily be inferred from the ones given below. Furthermore, results for three different values of n are given as a function of L at $\Lambda = 0.5$ in Figure 19, thus making it possible to infer results for those cases where the energy dependence of the particle distribution, as well as the flux level, changes with L value.

The computed E_T and F_p are shown in Figure 17. We have given results for L = 5, 4, 3, 2, and 1.5. In all cases the wave magnetic field intensity at the equator was taken to be 1 pT and wave pulse length was taken to be 400 m s. The format is similar to that of Figure 11, in fact the L = 4 cases of Figure 17 are identical to the n = 6 cases of Figure 11. The dotted lines in Figure 17 indicate the cases where the resonant particle energies are in the relativistic range (>150 keV). Since we have not included the relativistic correction in the equations of motion of the particles, these values are to be considered approximate.

It is interesting to note that the values given in Figure 17 represent the end result of the combined effects of varying inhomogeneity ($d\omega_H/dz$), cold plasma density (n_{eq}), and refractive index ($\mu = kc/\omega$) as we vary L at a fixed Λ or vice-versa. The results could be markedly different if Φ_E or n is allowed to change with L value.

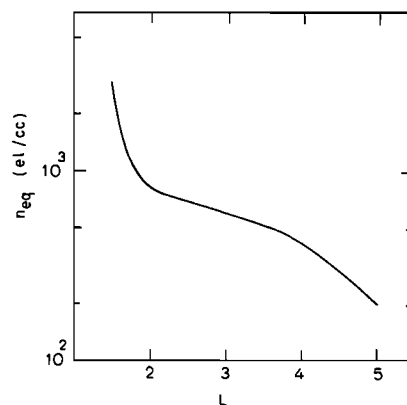In order to see the effect of the plasmapause, we compare the n_{eq} = 200 and 10 el/cc cases at

Fig. 16. Equatorial cold plasma density model used for the case study results shown in Figures 17, 18, 19, and 20.

L = 5, as shown in Figure 19. The result indicates that for these parameters and at Λ = 0.5, the peak flux F_p is less for the low-density case by about a factor of 2. It should be noted, however, that the peak flux for a typical inside-plasmapause case (at L = 4 and n_{eq} = 400 el/cc) and outside-plasmapause case (at L = 5 and n_{eq} = 10 el/cc) are about equal. The total energy E_T is seen to be reduced by a factor of 3 or 4, due mainly to the fact that the increased group velocity results in a precipitation pulse of shorter duration. This effect was also apparent in Figure 12.

The results in Figure 17 are for a distribution with n = 6. Figure 18 shows the dependence on n for the case of Λ = 0.5.

The results shown in Figure 17 can be used to obtain the value of the peak precipitation flux induced by a monochromatic wave of given frequency as a function of L value. Figure 20 shows the results for three frequencies, f = 5, 10.2, and 17.8 kHz, representing the typical operational frequencies of the Siple (SI) (Antarctica), Omega, North Dakota (ND), and the Cutler (NAA) (Maine) VLF transmitters, respectively. The values shown are obtained directly from the lower panel of Figure 17 and thus correspond to equatorial wave magnetic field intensities of B_w = 1 pT. For the cold plasma model of Figure 16 and for a constant value of Φ_E and n with L as assumed, the result defines the optimum L shell fro observing
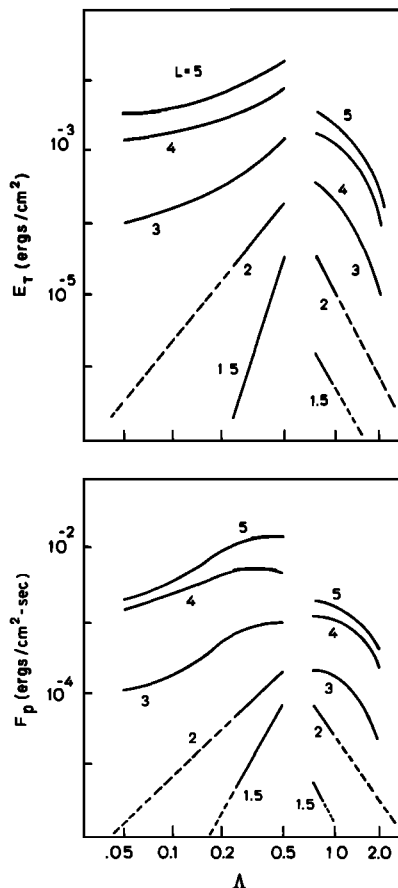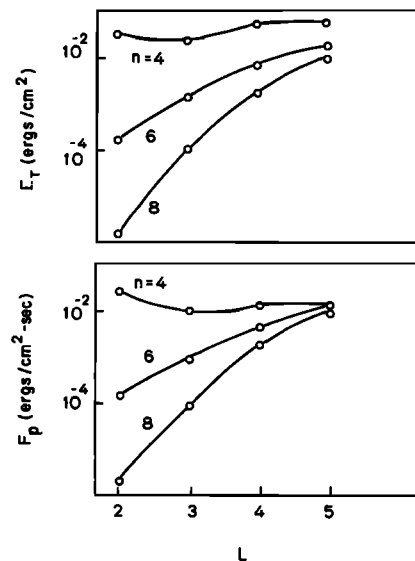

Fig. 18. Total deposited energy E_T and peak precipitated flux F_p as a function of Λ for L = 5. All other parameters having the same value as in Figure 17; the solid lines are for the case where n_{eq} = 200 el/cc and the dotted lines represent the case of n_{eq} = 10 el/cc.

precipitation at each frequency. For SI the optimum L shell is L = 4, whereas for NAA it is in the range of L = 3-4. For ND, the flux is more or less constant over L shells of 3-5.

For the specific cold plasma model of Figure 16, the energies of the particles that constitute the fluxes shown in Figures 17 and 18 are a function of L, n_{eq}, and Λ. The flux at any time is comprised of particles having a range of energies as is indicated by the lower panel of Figure 3. Figure 21 shows the lowest particle energies that comprise the peak fluxes shown in the lower panel of Figure 17. The energy spectra of the particles that comprise the peak is shown in Figure 22 for the two extreme cases of L = 2 and L = 5, both for Λ = 0.5. It can be seen that the maximum contribution to the flux comes from the lower-energy end of the spectra.

6. Summary and Conclusions

We have computed the electron flux precipitated out of the magnetosphere by relatively short VLf wave pulses under a broad range of magnetospheric conditions. The results clearly demonstrate the role of the energetic particle distribution function f(v,α), the normalized wave frequency Λ, L value of the path of propagation, cold plasma density n_{eq}, and wave intensity B_w. The precipitated energy flux in ergs/cm^2 s that would be observed at 1000-km altitude is presented as a function of time relative to the injection of the wave pulse at the same point. The energy range of the downcoming particles that constitute the flux is also shown. In this section we summarize our results and assumptions in relation to (1) the assumed wave structure, (2) L value and cold plasma density, (3) the energetic particle distribution function, and (4) detectability of the precipitated flux by existing instruments.
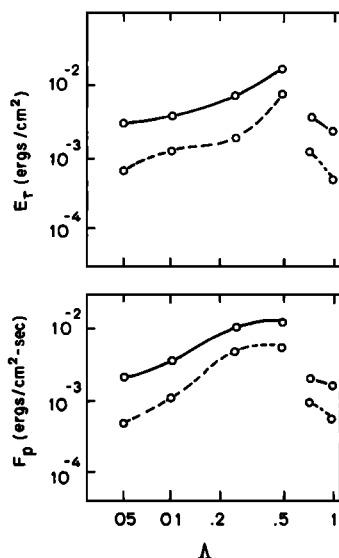

Fig. 17. Total deposited energy E_T and peak precipitated flux F_p as a function of normalized frequency Λ for L = 1.5, 2, 3, 4, and 5.

Fig. 19. Total deposited energy E_T and peak precipitated flux F_p as a function of L value for Λ = 0.5. All other parameters being the same as in Figure 17, results for the distribution function exponent n = 4, 6, and 8 are shown.

6.1. The Wave Structure

We have considered the case of a monochromatic, longitudinally propagating whistler mode wave pulse as described in (1). As discussed in section 2.1 we have computed the particle scatterings by using a pre-defined wave structure. It should be noted that when temporal growth of the wave occurs [Helliwell and Katsufrakis, 1974], then the wave intensity can be expected to increase as the wave crosses the equator. Since the temporal growth region is expected to be within a few degrees of the equator, the precipitated energy flux for such a case can be estimated by using our results that are computed by assuming a uniform wave amplitude distribution. The peak flux values given in the preceeding figures will not be significantly affected, since the peak flux is mostly due to contributions from particles that resonate with the wave after it crosses the equator. The shape of the precipitated flux versus time curves will change, but this change will be in a predictable manner, essentially amounting to a scaling down of the flux at the times when the contributions come from particles that resonate with the wave before it crosses the magnetic equator.

In addition, we have assumed sharp front and tail ends for the wave packet. We believe that this assumption is well justified, however, since even though dispersion effects will tend to produce a smoother front and tail structure, the resulting rise times will still be much shorter than typical wave-particle interaction times [Inan et al., 1978; Chang and Helliwell, 1980].

With these assumptions the monochromatic wave packet is uniquely defined by its center frequency, pulse length PL, and wave intensity as given in (1). The dependence of the particle scattering on wave frequency is demonstrated in Figures 7, 11, 17, 19, 20, and 21. In general, the

energy flux precipitated by a wave of given intensity B_w increases with wave frequency for Λ = f/f_{Heq} < 0.5 and decreases with wave frequency for Λ > 0.5. The energy of the particles that are near-resonant and that therefore are precipitated increases with decreasing frequency defined by (6).

The results shown in Figures 5 and 6 demonstrate the effect of wave pulse length PL. While the total deposited energy E_T increases with PL as expected, the peak flux remains approximately constant as PL is increased beyond a minimum value, which for L = 4 is about 400 m s. This result is important in the context of wave-injection experiments since it indicates that if the wave-induced precipitation is to be detected by techniques that respond to rapid variations in precipitation flux, (i.e., photometers, satellite detectors) then transmissions can be made at this minimum pulse length with high peak power levels. This consideration would be especially important for satellite-based VLF wave sources.

We have discussed the dependence on wave intensity in connection with Figure 14a. The precipitated flux is linearly proportional to B_w for values of B_w less than the upper limit B_u, as given in Figure 14b. The value of B_u is a function of L value, again as shown in Figure 14b. The typical unamplified intensities of manmade VLF transmitter signals in the magnetosphere would fall in the linear range [Inan et al., 1977; Bell et al., 1981]. However, after amplification and triggering, as often observed, the signals' levels would typically be closer to or higher than B_u. For natural emissions, such as VLF chorus, measured wave signal intensities are in the range of 1-100 pT [Burtis and Helliwell, 1975], and thus on occasion are larger than B_u. The results presented in this paper can be directly scaled up or down for estimating the flux levels precipitated by VLF wave pulses of intensity less than the B_u values given in Figure 14b.

Figure 8 shows the wave intensity at the equator for different values of Λ and for the same power density input at 1000-km altitude. The variation of B_w with Λ is independent of L value and is proportional to $n_{eq}^{1/2}$. This indicates that for wave injection experiments directed at pre-
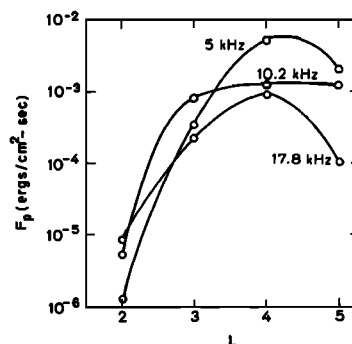

Fig. 20. The peak precipitated flux F_p versus L value for three different frequencies; 5 kHz representing typical operational frequency of the Siple transmitter (SI), 10.2 kHz representing the Omega, North Dakota (ND) transmitter, and 17.8 kHz representing the NAA transmitter in Cutler, Maine.

cipitating particles, operation at higher fre-
quencies and higher n_{eq} is desirable for achiev-
ing higher signal intensities at the equator for
the same total power input. Note, however, that
this consideration must be weighed against the
higher precipitation efficiency at higher L val-
ues (lower n_{eq}), as shown in Figure 17.

While we have limited our discussion in this
paper to the case of monochromatic waves, the
test particle simulation of the wave-particle
interaction is currently being extended to cover
the cases of interactions with waves of slowly
varying frequency. This extension will enable
us to predict more accurately the precipitation
levels that would be induced by natural signals
and triggered emissions. The results of this
study will be reported later.

6.2. L Value and Cold Plasma Density

The dependence of the precipitation on these
parameters were illustrated in Figures 12, 13, 17,
18, 19, and 21. In general, for typical cold
plasma density distributions in the magnetosphere,
the wave-induced precipitation flux is larger at
higher L shells and for higher n_{eq}. Figure 20
attempts to identify the optimum L shell for
observing precipitation induced by a wave of a
given frequency. One must be careful in applying
this criterion, however, since the results given
assume that the energetic particle distribution
$f(v,\alpha)$ and the differential energy spectrum Φ_E
is the same at all L values. This would not be
the case in general. The role of the distribu-
tion function is separately discussed below. The
relative flux levels at different L shells would
also depend on the cold plasma distribution
since this determines the energies of the near-res-
onant particles and therefore the efficiency of
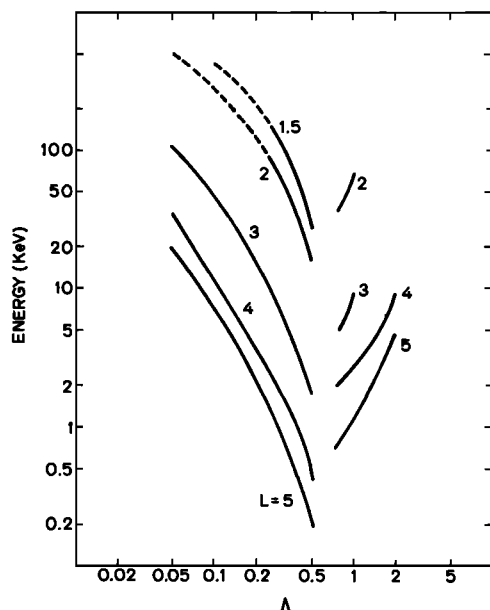the wave-particle interaction [Inan et al., 1978].

Fig. 21. The minimum energy of particles that
comprise the peak fluxes shown in Figure 17,
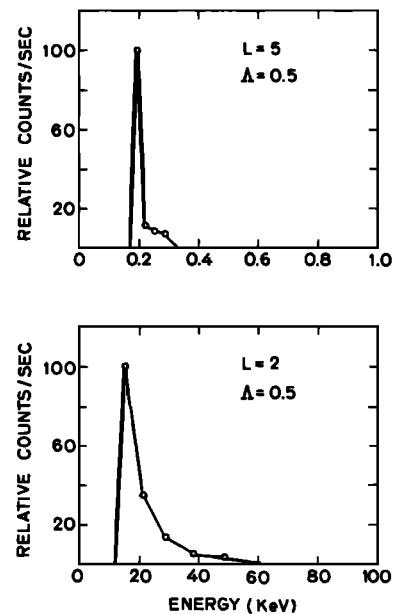given as a function of Λ for different values of
L.

Fig. 22. The energy spectra corresponding to the
peak fluxes for $\Lambda = 0.5$ and for L = 2 and 5.

For the case study (see Figure 16) discussed
above, we have found that the peak flux inside
(e.g., L = 4, n_{eq} = 400 el/cc) and outside
the plasmapause (e.g., L = 5, n_{eq} = 10 el/cc)
are about equal. However, the energies of the
downcoming particles that constitute the flux
are much larger for the latter case.

6.3. The Energetic Particle Distribution $f(v,\alpha)$

We have considered initial trapped particle
distribution functions that are defined by (4)
and (5). By proper choice of $g(\alpha)$, n and Φ_E,
one can match the function defined by (5) to most
observed energetic particle distributions in the
magnetosphere [Schield and Frank, 1970; Anderson,
1976].

For most of the results presented in this pap-
er we have used an isotropic distribution for
which $g(\alpha)$ = 1. For anisotropic distributions
peaked around α = 90°, and for which $g(\alpha)$ is flat
for a few degrees above the loss cone, the flux
values would be reduced by a factor $g(90°)/g(\alpha_{\ell c})$,
where $\alpha_{\ell c}$ is the half-angle of the loss cone
[Inan et al., 1978]. The case of distribution
functions with anisotropy in the vicinity of the
loss cone was discussed in Figure 15.

We have given results for n = 4, 6, and 8.
The dependence of precipitation on this parameter
is discussed in connection with Figures 10, 11,
and 19. We have shown in Figure 10 that the
characteristic shape of the precipitation pulse
is a function of n. This result is important
because it indicates that if controlled precipi-
tation of energetic particles from the magneto-
sphere can be achieved, the observed temporal
behavior of the flux can possibly be used for
diagnosing the details of the energetic particle
distribution function. It should be noted, how-
ever, that the variation of the wave amplitude
across a given duct, and also the spatial ampli-
tude variations due to wave-growth effects may

TABLE 1. Minimum Detectable Precipitated Energy Flux

Detector	Precipitated Energy Flux Threshold/ ergs/cm^2-s	Reference
Human eye at 5577 Å	5.0	Omholt [1971]
Photography	2.5	Jones [1974]
Satellite and rocket particle detector (scintillation type)	3.8×10^{-3}	Hargreaves and Sharp [1965]
Photometer 4278 Å	2.5×10^{-3}	S. B. Mende (private communication, 1981)
HF Sounder kinesonde phase	10^{-3}	J. H. Doolittle (private communication, 1981)
Balloon x rays (scintillation detector)	5×10^{-3}	Rosenberg et al. [1971b]
Riometer, 30 MHz	2.5×10^{-3}	Rosenberg et al. [1971]; Hargreaves and Sharp [1965]
SEEP satellite particle detector	10^{-4}-10^{-5}	W. L. Imhof (private communication, 1981)

tend to degrade the sensitivity of this diagnostic method.

The precipitated energy flux values given in this paper are directly proportional to the differential energy spectrum of the trapped energetic particles, i.e., Φ_E. For most of the results presented we have used $\Phi_E = 10^8$ el/cm^2 s sr keV, representing the differential energy spectrum of E = 1 keV particles at α = 90° pitch angle. Furthermore, we have assumed no variation of this quantity with L value.

The value that we have used for Φ_E is typical of the flux levels outside and just inside the plasmapause during geomagnetically disturbed times [Schield and Frank, 1970; Anderson, 1976]. Flux levels observed during quiet times are in the range of 10^6-10^8 el/cm^2 s sr keV [Lyons and Williams, 1975]. Recent measurements on the Dynamics Explorer satellite indicate that the flux levels are highly variable with L shell, geomagnetic conditions, and local time but agree with typical levels of 10^6-10^8 el/cm^2 s sr keV [D. Winningham, private communication, 1982].

It should also be noted that the relative magnitudes of the precipitated fluxes at different L shells as given in Figures 13, 17, 19, and 21 are based on an assumed constant value of Φ_E with L. Because of the highly variable nature of Φ_E we have chosen to present our results with this assumption. For any realistic variation of Φ_E as a function of L, the precipitated flux values can be obtained from the results given by proper scaling.

6.4. Detectability of the Wave-Induced Precipitated Flux

For the assumed values of the parameters (including Φ_E), we have computed and presented absolute levels of the precipitated energy flux. The results range from 10^{-6}-10^{-1} ergs/cm^2 s for particles of 0.3-100 keV. The detectability of this flux by existing instruments would depend on (1) the relative values of typical background drizzle-type of precipitation at these latitudes and (2) the sensitivity of the instruments.

The background precipitation levels at mid-latitude and the particle energies of interest (1-100 keV) are in the 10^{-6}-10^{-4} ergs/cm^2 s range, with the higher levels observed during geomagnetically disturbed times [Voss and Smith, 1980]. Thus the flux values that we have estimated are typically 10^2-10^3 times larger than this background and should be detectable if the instruments have enough sensitivity.

The sensitivity of various existing techniques for detecting precipitation fluxes (or ionospheric effects produced by them) was recently reviewed [Doolittle, 1982]. The results shown in Table 1 are partly adopted from this work and summarize the minimum precipitated energy flux detectable by various techniques. For Φ_E = 10^8 el/cm^2 s sr keV, most of the flux values reported in this paper are detectable by these presently available instruments. It should be noted again that the flux values are proportional to Φ_E as well as B$_W$. The results shown in Figure 17 are

for B_w = 1 pT. For ground-based sources, the magnetic field intensity at the equatorial plane would depend on the radiated power, proximity of the injection point to the source, propagation conditions and availability of ducts, and the possible amplification of the signal due to gyro-resonance interactions. As an example, the intensity of nonducted Siple transmitter signals (radiated power ~2 kW) at the magnetic equator, and before amplification, was measured to be in the 0.1-0.3 pT range [Inan et al., 1977; Bell et al., 1981]. However, 30-40 dB amplification of the transmitter signals and triggering of emissions is often observed [Helliwell and Katsufrakis, 1974].

The characteristic shape of the precipitation pulses might also be useful in detecting these events. Knowledge of the expected pulse shape might be used to 'match' the filter characteristics to the signal shape.

References

Anderson, R. R., Wave particle interactions in the evening magnetosphere during geomagnetically disturbed periods, Ph.D. thesis, Univ. of Iowa, Iowa City, 1976.

Angerami, J. J., A whistler study of the distribution of thermal electrons in the magnetosphere, Tech. Rep. 3412-7, Radiosci. Lab., Stanford Univ., Stanford, Calif., 1966.

Angerami, J. J., and J. O. Thomas, Studies of planetary atmospheres, 1, The distribution of electrons and ions in the earth's exosphere, J. Geophys. Res., 69, 4537, 1964.

Ashour-Abdalla, M., Amplification of whistler waves in the magnetosphere, Planet. Space Sci., 20, 639, 1972.

Banks, P. M., C. R. Chappell, and A. F. Nagy, A new model for the interaction of auroral electrons with the atmosphere: Spectral degradation, backscatter, optical emission, and ionization, J. Geophys. Res., 79, 1459, 1974.

Bell, T. F., and U. S. Inan, Transient nonlinear pitch angle scattering of energetic electrons by coherent VLF wave packets in the magnetosphere, J. Geophys. Res., 86, 9047, 1981.

Bell, T. F., U. S. Inan, and R. A. Helliwell, Nonducted coherent VLF waves and associated triggered emissions observed on ISEE 1 satellite, J. Geophys. Res., 86, 4649, 1981.

Burtis, W. J., and R. A. Helliwell, Magnetospheric chorus: Amplitude and growth rate, J. Geophys. Res., 80, 3265, 1975.

Carpenter, D. L., and T. R. Miller, Ducted mag-

netospheric propagation of signals from the Siple, Antarctica, VLF transmitter, J. Geophys. Res., 81, 2692, 1976.

Chang, D. C. D., and R. A. Helliwell, Emission triggering in the magnetosphere by controlled interruption of coherent VLF signals, J. Geophys. Res., 84, 7170, 1979.

Chang, D. C. D., and R. A. Helliwell, VLF pulse propagation in the magnetosphere, IEEE Trans. Antennas Propag., AP-28, 170, 1980.

Das, A. C., A mechanism for VLF emissions, J. Geophys. Res., 76, 6915, 1971.

Dingle, B., and D. L. Carpenter, Electron precipitation induced by VLF noise bursts at the plasmapause and detected at conjugate ground stations, J. Geophys. Res., 86, 4597, 1981.

Doolittle, J. H., Modification of the ionosphere by VLF wave-induced electron precipitation, Ph.D. thesis, Stanford Univ., Stanford, Calif., 1982.

Dowden, R. L., A. C. McKey, L. E. S. Amon, H. C. Koons, and M. H. Dazey, Linear and nonlinear amplification in the magnetosphere during a 6.6-mHz transmission, J. Geophys. Res., 83, 169, 1978.

Dungey, J. W., Loss of Van Allen electrons due to whistlers, Planet. Space Sci., 11, 591, 1963.

Dungey, J. W., Effects of electromagnetic perturbations on particles trapped in the radiation belts, Space Sci. Rev., 4, 199, 1964.

Gendrin, R., Pitch angle diffusion of low energy protons due to gyroresonant interaction with hydromagnetic waves, J. Atmos. Terr. Phys., 30, 1313, 1968.

Gendrin, R., Phase bunching and other non-linear processes occurring in gyroresonant wave-particle interactions, Astrophys. Space Sci., 28, 245, 1974.

Hargreaves, J. K., and R. D. Sharp, Electron precipitation and ionospheric radio absorption in the auroral zones, Planet. Space Sci., 13, 1171, 1965.

Helliwell, R. A., Whistlers and Related Ionospheric Phenomena, Stanford University Press, Stanford, Calif., 1965.

Helliwell, R. A., A theory of discrete VLF emissions from the magnetosphere, J. Geophys. Res., 72(19), 4773, 1967.

Helliwell, R. A., Controlled VLF wave injection in the magnetosphere, Space Sci. Rev., 15, 781, 1974.

Helliwell, R. A., Active very-low-frequency experiments on the magnetosphere from Siple Station, Antarctica, Phil. Trans. R. Soc. London Ser. B., 279, 213, 1977.

Helliwell, R. A., and J. P. Katsufrakis, VLF wave injection into the magnetosphere from Siple Station, Antarctica, J. Geophys. Res., 79, 2511, 1974.

Helliwell, R. A., and J. P. Katsufrakis, Controlled wave-particle interaction experiments, in Upper Atmosphere Research in Antarctica, Antarctic Res. Ser., vol. 29, edited by L. J. Lanzerotti and C. G. Park, AGU, Washington, D.C., 1978.

Helliwell, R. A., J. P. Katsufrakis, and M. L. Trimpi, Whistler-induced amplitude perturbation in VLF propagation, J. Geophys. Res., 78, 4679, 1973.

Helliwell, R. A., S. B. Mende, J. H. Doolittle,

W. C. Armstrong, and D. L. Carpenter, Correlations between λ4278 optical emissions and VLF wave events observed at L ~ 4 in the Antarctic, J. Geophys. Res., 85, 3376, 1980a.

Helliwell, R. A., D. L. Carpenter, and T. R. Miller, Power threshold for growth of coherent VLF signals in the magnetosphere, J. Geophys. Res., 85, 3360, 1980b.

Hoffman, R. A. (Ed.), Dynamics Explorer, D. Reidel, Hingham, Mass., 1981.

Imhof, W. L., E. E. Gaines, and J. B. Reagan, Evidence for the resonance precipitation of energetic electrons from the slot region of the radiation belts, J. Geophys. Res., 79, 3141, 1974.

Imhof, W. L., R. R. Anderson, J. B. Reagan, and E. E. Gaines, The significance of VLF transmitters in the precipitation of inner belt electrons, J. Geophys. Res., 86, 11225, 1981.

Inan, U. S., and T. F. Bell, The plasmapause as a VLF wave guide, J. Geophys. Res., 82, 2819, 1977.

Inan, U. S., T. F. Bell, D. L. Carpenter, and R. R. Anderson, Explorer 45 and Imp 6 observations in the magnetosphere of injected waves from the Siple Station VLF transmitter, J. Geophys. Res., 82, 1177, 1977.

Inan, U. S., T. F. Bell, and R. A. Helliwell, Nonlinear pitch angle scattering of energetic electrons by coherent VLF waves in the magnetosphere, J. Geophys. Res., 83, 3235, 1978.

Kennel, C. F., Consequences of a magnetospheric plasma, Rev. Geophys. Space Phys., 7, 379, 1969.

Kennel, C. F., and H. E. Petschek, Limit on stably trapped particle fluxes, J. Geophys. Res., 71, 1, 1966

Koons, H. C., B. C. Edgar, and A. L. Vampola, Precipitation of inner zone electrons by whistler mode waves from the VLF transmitters UMS and NWC, J. Geophys. Res., 86, 640-648, 1981.

Lockheed Palo Alto Research Laboratory, Proposal to implement a stimulated emission of energetic particles (SEEP) experiment, LMSC/D682347, October 1979.

Lyons, L. R., Comments on pitch-angle diffusion in the radiation belts, J. Geophys. Res., 78, 6793, 1973.

Lyons, L. R., General relations for particle diffusion in pitch angle and energy, J. Plasma Phys., 12, 45, 1974a.

Lyons, L. R., Pitch angle and energy diffusion coefficients from resonant interactions with ion-cyclotron and whistler waves, J. Plasma Phys., 12, 417, 1974b.

Lyons, L. R., and D. J. Williams, The quiet time structure of energetic (35-560 keV) radiation belt electrons, J. Geophys. Res., 80, 943, 1975.

Mende, S. B., R. L. Arnoldy, L. J. Cahill, Jr., J. H. Doolittle, W. C. Armstrong, and A. C. Fraser-Smith, Correlation between λ4278-Å optical emissions and a Pc 1 pearl event observed at Siple Station, Antarctica, J. Geophys. Res., 85, 1194, 1980.

Park, C. G., Generation of whistler-mode sidebands in the magnetosphere, J. Geophys. Res., 82, 2286, 1981.

Raghuram, R., T. F. Bell, R. A. Helliwell, and J. P. Katsufrakis, Echo-induced suppressions of coherent VLF transmitter signals in the

magnetosphere, J. Geophys. Res., 82, 2787, 1977.

Rees, M. H., Auroral ionization and excitation by incident energetic electrons, Planet. Space Sci., 11, 1209, 1963.

Roberts, C. S., Electron Loss from the Van Allen zones due to pitch angle scattering by electromagnetic disturbances, in Radiation Trapped in the Earth's Magnetic Field, edited by B. M. McCormac, pp. 403-421, D. Reidel, Hingham, Mass., 1966.

Roberts, C. S., Cyclotron resonance and bounce resonance scattering of electrons. trapped in the earth's magnetic field, in Earth's Particles and Fields, edited by B. M. McCormac, pp. 317-336, Reinhold, New York, 1968.

Roberts, C. S., Pitch angle diffusion of electrons in the magnetosphere, Rev. Geophys. Space Phys., 7, 305, 1969.

Roederer, J. G., Dynamics of Geomagnetically Trapped Particles, Springer, New York, 1970.

Rosenberg, T. J., R. A. Helliwell, and J. P. Katsufrakis, Electron precipitation associated with discrete very-low-frequency emissions, J. Geophys. Res., 76, 8445, 1971a.

Rosenberg, T. J., J. Bjordal, H. Trefall, G. J. Kvifte, A. Omholt, and A. Egeland, Correlation study of auroral luminosity and X rays, J. Geophys. Res., 76, 122, 1971b.

Rosenberg, T. J., J. C. Siren, D. L. Matthews, K. Marthinsen, J. A. Holtet, A. Egeland, D. L. Carpenter, and R. A. Helliwell, Conjugacy of electron microbursts and VLF chorus, J. Geophys. Res., 86, 5819, 1981.

Schield, M. A., And L. A. Frank, Electron observations between the inner edge of the plasma sheet and the plasmasphere, J. Geophys. Res., 75, 5401, 1970.

Schulz, M., and L. J. Lanzerotti, Particle Diffusion in the Radiation Belts, Springer, New York, 1973.

Smith, R. L., R. A. Helliwell, and I. W. Yarbroff, A theory of trapping of whistlers in field-aligned columns of enhanced ionization, J. Geophys. Res., 65, 1839, 1960.

Tsuruda, K., S. Machida, T. Terasawa, A. Nishida, and K. Maezawa, High spatial attenuation of the Siple transmitter signal and natural VLF chorus observed at ground-based chain stations near Roberval, Quebec, J. Geophys. Res., 87, 742, 1982.

Tsurutani, B. T., and E. J. Smith, Postmidnight chorus: A substorm phenomenon, J. Geophys. Res., 79, 118, 1974.

Vampola, A. L., and G. A. Kuck, Induced precipitation of inner zone electrons, 1, Observations, J. Geophys. Res., 83, 2543, 1978.

Voss, H., and L. G. Smith, Global zones of energetic particle precipitation, J. Atmos. Terr. Phys., 42, 227, 1980.

Walt, M., W. M. MacDonald, and W. E. Francis, Penetration of auroral electrons into the atmosphere, in Physics of the Magnetosphere, edited by R. L. Carovillano, pp. 534-555, D. Reidel, Hingham, Mass., 1969.